IL-6 SIGNALING EXACERBATES HALLMARKS OF CHRONIC TENDON DISEASE BY STIMULATING PROGENITOR PROLIFERATION & MIGRATION TO DAMAGE.

Tino Stauber, Greta Moschini, Amro A. Hussien, Patrick K. Jaeger, Katrien De Bock, Jess G. Snedeker

University of Zurich, Department of Orthopedics
ETH Zurich, Institute for Biomechanics
Lengghalde 5, 8008 Zurich, Switzerland
E-mail: jess.snedeker@hest.ethz.ch

Laboratory of Exercise and Health
Department of Health Sciences and Technology (D-HEST)
ETH Zurich, Swiss Federal Institute of Technology

Keywords: tendon, interleukin-6, progenitors, assembloid

ABSTRACT:

Tendinopathies are debilitating diseases currently increasing in prevalence and associated costs. There is a need to deepen our understanding of the underlying cell signaling pathways to unlock effective treatments. In this work, we screen cell signaling pathways in human tendinopathies and find enriched IL-6/JAK/STAT signaling alongside signatures of cell populations typically activated by IL-6 in other tissues. To dissect the underlying causalities, we combine IL-6 knock-out mice with an explant-based assembloid model of tendon damage to successfully connect IL-6 signaling to fibroblast progenitor activation and recruitment. Vice versa, we show that these fibroblast progenitors promote the development of tendinopathy hallmarks in the damaged explant upon IL-6 activation. Finally, we present in vivo data confirming diminished migration of progenitors to acute Achilles tendon lesions in IL-6 knock-out mice. We conclude that IL-6 activates tendon tissues to initiate normal healing processes that can deteriorate into tendinopathy hallmarks.

INTRODUCTION

Tendons are essential to every human movement.[1] Tendinopathies represent the largest group of common tendon diseases and approximately 22% of all sport-related injuries.[2] They can strike tendons at many different anatomical locations, can dramatically diminish quality of life by limiting the associated movements, and often share a history of repetitive overuse-induced damage and repair cycles.[2–5] Once adult tendon regions fail to keep up with functional demands, they fall into a state of non-resolving, uncontrolled lesion repair.[6–12]

These chronic tendon lesions underlying tendinopathies feature characteristics of normal wound healing including accelerated extracellular matrix turnover and proliferation of (fibroblast) progenitor populations as well as their migration to replace and repopulate damaged tissues.[12–17] In tendon, (e.g. Scx$^+$) progenitor populations are assumed to reside primarily in the extrinsic compartment comprising epitenon and paratenon from where they are recruited to the damaged intrinsic compartment embodied by the load-bearing tendon core.[15,18–21] While the mechanisms governing tendon progenitor activation, proliferation, and recruitment are unclear, some insight can be gleaned from studies on other musculoskeletal tissues.[4,22]

In acute muscle lesions, mechanisms for repair, hypertrophy, and hyperplasia are dominated by the satellite cells residing in the muscle basal lamina.[23–26] Satellite cells in muscle and dermal fibroblasts in skin are mainly activated and recruited by interleukin-6 (IL-6), a key player in the acute phase response to stress.[23,26,27] Stress-related mechanisms activating *IL-6* mRNA transcription in the absence of exogenous pathogens include damage-associated molecular patterns (DAMPs), calcium signaling after membrane-depolarization, but also energetic stressors like glycogen depletion and redox signaling following exercise.[28,29] In humans, IL-6 transmits its signal via classical or trans-signaling.[30] Classical signaling involves the membrane-bound receptor IL6R, which forms a homodimer with gp130 upon IL-6 binding. Trans-signaling works similarly, except that the IL6R has been solubilized (sIL6R) by metalloproteases (mostly ADAM10 & 17)[31], which cleave it from the cell membrane.[30,31] Since not all cell populations express IL6R, trans-signaling via sIL6R enables IL-6 signaling for a wider range of cell populations. Regardless of classical or trans-signaling initiation, further transduction of the IL-6 signal runs via two major pathways (JAK/STAT/ERK[32,33] & SHP2/Gab/MAPK[34,35]) to turn on cellular processes inducing proliferation, migration, metabolic adaptations, and tissue turnover.[30,36] In chronic muscle lesions like Duchenne muscular dystrophy, IL-6 is persistently upregulated, and anti-IL-6 receptor antibodies have been proposed as treatment options.[37] Anti-IL-6 receptor antibodies (IL-6 inhibitors) like Tocilizumab inhibit both classical and trans-signaling and are routinely used in other chronic inflammatory diseases like systemic sclerosis, psoriasis, and rheumatoid arthritis.[28,38–42] In this context, IL-6 inhibitors have been shown to reduce disease-hallmarks including arthritis-concomitant tendon inflammation.[43–45] Analogous to these chronic inflammatory musculoskeletal diseases, tendinopathies present with localized pain, swelling, and functional decline in the affected organ.[4,7,46,47] Histological and molecular characteristics of tendinopathy include hypercellularity, disorganized collagen fibers including mechanically inferior collagen-3, and dysregulated extracellular matrix homeostasis.[14,48–50]

Here, we investigated the hypothesis that IL-6 plays a vital role in activating fibroblast progenitor proliferation within the extrinsic tissue compartment (i.e. tendon sheath or synovial membranes) and recruitment of these cells to the damaged tendon core tissue.[12,51–53] While this likely

represents a critical step in normal tendon healing[54–56], we further propose that extended and excessive IL-6 signaling may causally exacerbate tendinopathy through the same mode of action.[57]

We experimentally tested and confirmed these hypotheses in three steps:

1) We showed that the IL-6/JAK/STAT signaling cascade is enriched in human tendinopathic tendons alongside gene signatures typical for fibroblasts and progenitors as well as downstream gene sets suggesting excessive cell proliferation (hypercellularity) and imbalanced extracellular matrix turnover.

2) We exploited an explant-based assembloid model system to first confirm the causal effect of IL-6 signaling on extrinsic fibroblast progenitor activation, recruitment, and proliferation. We then found additional *in vivo* support for IL-6 dependent recruitment of Scx^+ fibroblast populations using an Achilles tendon lesion model in IL-6 KO mice.

3) We followed the downstream effects of enhanced extrinsic fibroblast progenitor activation and accumulation on the tendon core embedded in our assembloids. Here, we document the emergence of central tendinopathic hallmarks including aberrant (catabolic) matrix turnover, hypercellularity, and hypoxic responses with a stronger fibroblast progenitor presence, which is reduced when IL-6 core signaling is inhibited.

RESULTS

The IL-6/JAK/STAT signaling signature is enriched in human tendinopathic tendons alongside signatures of extrinsic cell population activation and hallmarks of clinical tendinopathy.

To better illuminate the ongoing wound healing processes that are a central feature of chronic tendon disease, we first searched for enriched signaling pathways underlying tendinopathic tendons in a publicly available dataset (GEO: GSE26051).[58] To deduce common disease patterns affecting tendons from diverse anatomical locations, the microarray dataset contained analyzed samples from 23 healthy and 23 lesional human tendons of mixed anatomical origin. We excluded 7 healthy and 6 tendinopathic subjects identified as outliers after principal component analysis (**Supplementary Table 1 & Supplementary Figure 2**). Overall, we found 1488 significantly upregulated genes, 1788 significantly downregulated genes, and 18623 not-differentially regulated genes in tendinopathic compared to healthy control tendons.

Transcript	Effect size	P-value
IL-6	1.9	0.002
IL6Rα	-0.5	0.07
IL6ST / GP130	0.09	0.6
ADAM10	0.56	0.01
ADAM17	0.4	0.18
JAK1	0.6	0.01
STAT1	0.7	0.002
STAT3	0.71	0.001
MAPK3	-0.93	0.0002
GAP2	-0.88	0.002
IL-11	1.4	0.03
IL11R	-0.3	0.3
OSM	-0.9	0.04
OSMR	1.04	0.014
LIF	0.25	0.7
LIFR	1	0.028
COL1A1	1	0.0004
COL3A1	0.75	0.007
MMP9	2.37	0.003
MMP13	1.71	0.02
MMP3	-2.67	0.006

Table 1: Effect sizes and p-values for selected transcripts. The data describes the differences between tendinopathic and healthy control human tendons.

Further analysis revealed significantly upregulated *IL-6* transcripts in tendinopathic tendon tissue (**Figure 1A & B, Table 1**). Conversely, *IL-6* receptor (*IL6Rα*) expression trended toward downregulation and *IL-6* signaling transducer (*IL6ST,* also known as *GP130*) expression remained unchanged. Focusing on proteases that generate soluble *IL6Rα*, we found significant upregulation of *ADAM10* and a trend toward upregulated *ADAM17* in human tendinopathic tendons. Downstream of *IL-6* receptor binding, *JAK1* as well as *STAT1/3* were significantly upregulated. Other *IL-6* regulated signaling checkpoints included downregulated expression of *MAPK3* and *GAP2*. Aside from *IL-6*, other members of the IL-6 family were significantly dysregulated as well, including interleukin-11 (IL-11) and oncostatin M (*OSM)*.

In line with aberrant matrix turnover generally featured in tendinopathy, the transcripts of the following genes were significantly increased in the tendinopathic samples: *COL1A1*, *COL3A1*, *MMP9*, *MMP13*.

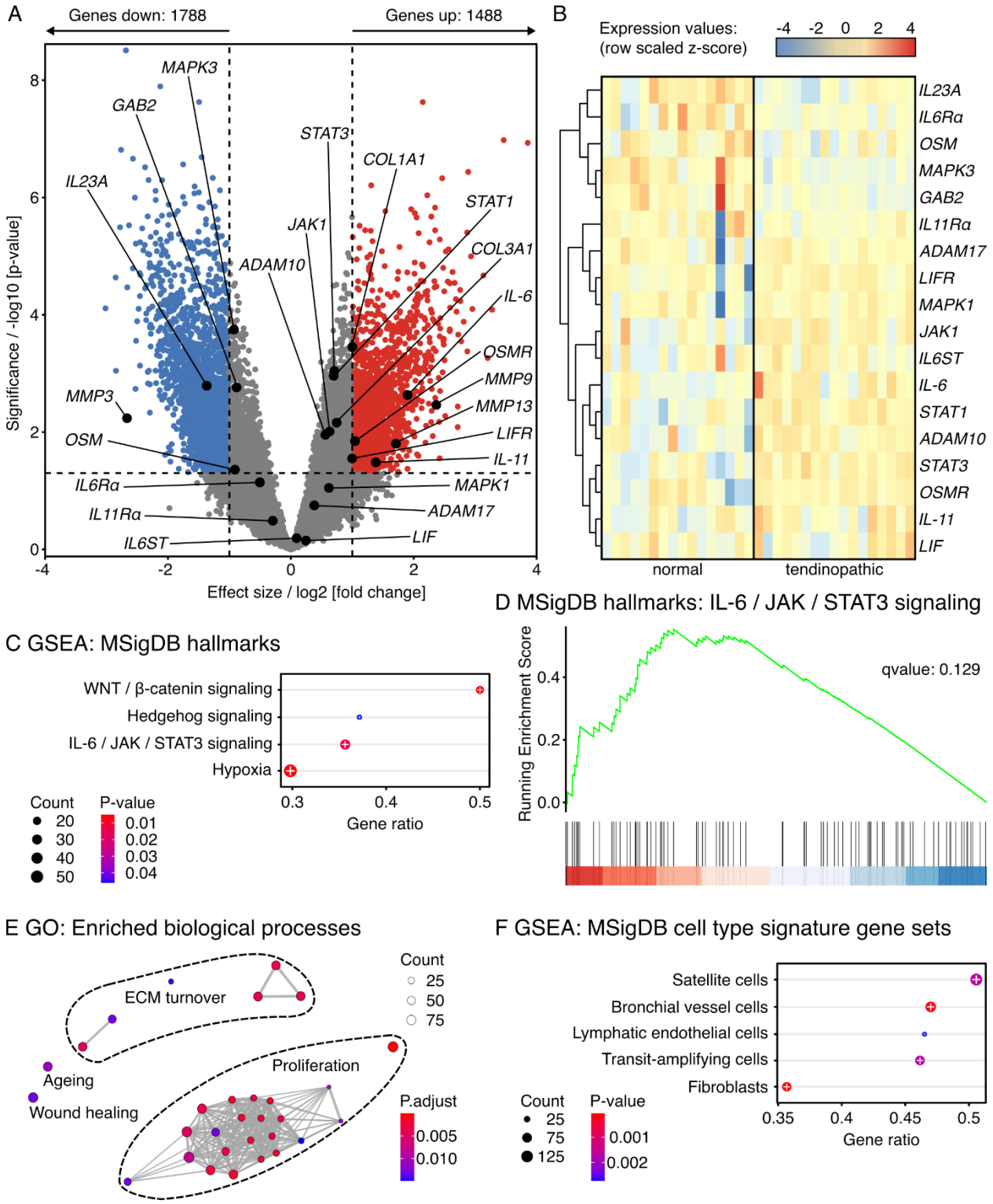

Figure 1: Transcriptome analysis of up- and downregulated genes and pathways in normal and human tendinopathic tendons. (A) Volcano plot of differentially expressed genes (DEGs) comparing tendinopathic to normal human tendons. Genes colored in red have a log2 (fold change) > 1, a p-value < 0.05, and are therefore considered to be significantly increased. Genes colored in blue have a log2 (fold change) < -1, a p-value < 0.05, and are therefore considered to be significantly decreased. The log2 and p-value thresholds are represented by the dashed lines. Annotated genes are part of the IL-6 cytokine superfamily, the IL-6 signaling cascade, or involved in matrix turnover.

(B) Unsupervised hierarchical clustering of expression values from members of the IL-6 cytokine superfamily, their receptors, and parts of the IL-6 signaling cascade (N=16 normal, N=17 tendinopathic). Genes are clustered by color with positive (red) or negative (blue) row-scaled z-scores. (C) Dotplot showing significantly enriched gene sets (p-value < 0.05) as determined by GSEA based on the MSigDB human hallmark gene sets. The color of the circles represents their p-value, the size the number of enriched genes (count), the position on the x-axis the number of enriched genes in ratio to the total number of genes annotated to the gene set (gene ratio), and the +/- signs the direction of the enrichment. (D) GSEA plot for the IL-6/JAK/STAT3 signaling hallmark contained in the MSigDB human hallmark gene sets. The green line traces the running enrichment score on the y-axis while going down the rank of genes listed on the x-axis. (E) Enrichment map plot clustering the top 30 biological processes significantly enriched by overlapping DEG sets. The color of the circles represents their adjusted p-value, the size represents the number of enriched genes (count), and the grey lines connect GO annotations that share the same gene subsets. The manually mapped cluster borders are indicated by dashed lines and the detailed annotations are listed in the **Supporting Figure 3** (F) Dotplot showing significantly enriched gene sets (p-value < 0.05) as determined by GSEA based on the MSigDB human cell type signature gene sets. The color of the circles represents their p-value, the size the number of enriched genes (count), the position on the x-axis the number of enriched genes in ratio to the total number of genes annotated to the gene set (gene ratio), and the +/- signs the direction of the enrichment.

Since changes in single transcripts alone have a limited predictive value for pathway-level changes, we next performed unbiased gene set enrichment analysis (GSEA) using the human hallmark dataset from MSigDB.[59,60] Confirming the trends from the single transcript analysis, GSEA revealed a positive enrichment of the IL-6/JAK/STAT pathway (qvalue: 0.129) alongside WNT / β-catenin, hedgehog, and hypoxic signaling (**Figure 1C & D**). We then looked further into changed biological processes by mapping the significantly changed single transcripts (p-value < 0.01) to the respective gene ontology (GO) database in an overrepresentation analysis (ORA). The resulting enrichment map plot (emapplot, **Figure 1E & Supplementary Figure 3)** depicting the top 200 enriched biological processes in clusters highlighted proliferation and extracellular matrix (ECM) turnover, which are known hallmarks of both wound healing and tendinopathy. Lastly, we attributed the detected transcript changes to cell types typically inducing them by exploiting the human cell type signature gene sets from MSigDB in an unbiased GSEA.[59,60] While this database does not yet include tendon-specific cell populations, it mapped the transcript change signatures to the following archetypes: multipotent progenitor cells (satellite & transit-amplifying cells), cells forming vascular networks (bronchial vessel & lymphatic endothelial cells), and fibroblasts (**Figure 1F**). Based on research performed in other tissues, progenitor cells and fibroblasts are prime targets and effectors for IL-6 signaling in a wound healing context.[27,61–63]

We conclude from the above analysis that IL-6 signaling in tendinopathic tendons plausibly contributes to chronic tendinopathic hallmarks like hypercellularity and aberrant matrix turnover, potentially by activating fibroblast progenitor cell populations. On this basis, we sought to directly test whether a causal relationship exists between the observed changes in IL-6 signaling and the associated disease processes. To this end, we harnessed an *in vitro* assembloid model of inter-compartmental crosstalk to better dissect the role of IL-6 in tendinopathy.

IL-6 signaling by tendon core explants activates extrinsic fibroblast progenitors.

We have previously validated a hybrid explant // hydrogel assembloid model that reproduces the *in vivo* tissue compartment interface between the load-bearing tendon core and the synovium-like extrinsic compartment (i.e. tendon sheath).[51] We exploited this model to test whether IL-6 signaling across tissue compartments could activate fibroblast progenitor cells in the peritendinous space in a manner that mimics the IL-6 signaling signatures we uncovered in the human data analysis (**Figure 2A**). Briefly, we isolated and clamped mouse tail tendon fascicles

to represent the tendon core while selecting (mainly Scx⁺ and CD146⁺) fibroblast progenitors from digested Achilles tendons based on plastic adherence growth as established previously (**Figure 2B & C**).[51,64] To form the artificial extrinsic compartment, we encapsulated these fibroblast progenitor populations into a collagen hydrogel which we then let polymerize around the clamped core explants. To dissect the effect of IL-6 signaling on these extrinsic target populations, we integrated either wildtype-derived (WT) or IL-6 knock-out-derived (KO) explants from the B6.129S2-Il6^{tm1Kopf}/J[65] mouse line. We then performed bulk RNA-sequencing on the extrinsic populations after one week of co-culture (**Figure 3A**).

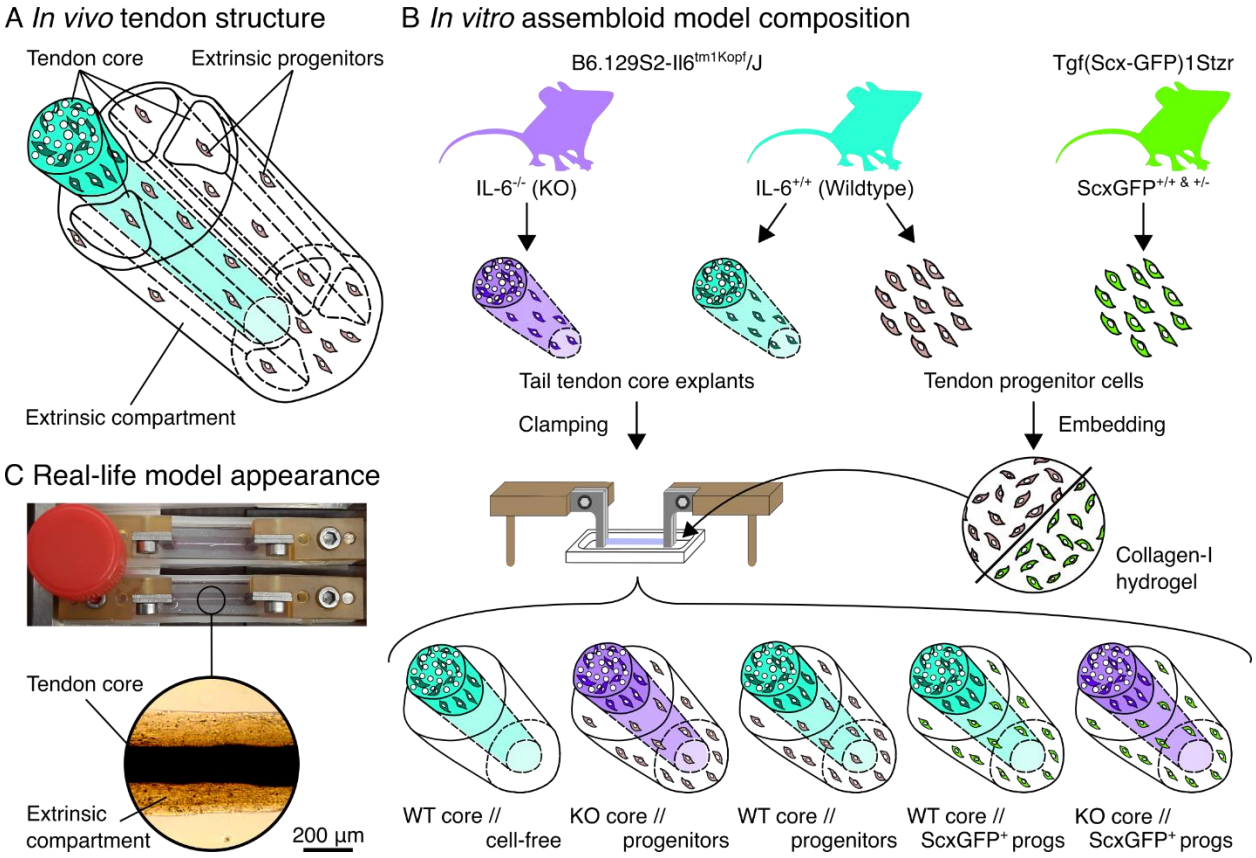

Figure 2: Concept behind the in vitro hybrid explant // hydrogel assembloid system. (A) Abstract representation of the in vivo load-bearing tendon core subunits (light blue / white) surrounded by the extrinsic compartment (white) containing i.e. extrinsic fibroblast progenitors (light brown). (B) Sources of the in vitro model system components with the IL-6 knock-out core (KO core) in violet, the IL-6 wildtype core (WT core) in light blue, the IL-6 wildtype fibroblast progenitors in light brown, and the ScxGFP+ fibroblast progenitors in green. Core explants were clamped and the fibroblast progenitors embedded in a (liquid) collagen solution before crosslinking the mixture into a hydrogel around the clamped core explants in various combinations. (C) Photographic and light microscopic images of the in vitro assembloid model system. Lid of a 15 ml Falcon® tube (Ø: 17 mm) used for scale.

Overall, integration of an IL-6 KO core increased transcripts of 256 genes in the surrounding extrinsic compartment, decreased transcripts of 98 genes, and left 15'295 unchanged (**Figure 3B & C)**. After mapping the significant transcript changes to biological processes in the GO database, we conducted a biased search for processes matching those dysregulated in human tendinopathic tendons. Out of the 195 significantly enriched biological processes (adjusted p-value < 0.05), 10 (5.1%) could be linked to changes in local cellularity and another 10 to ECM turnover (**Figure 3D**).

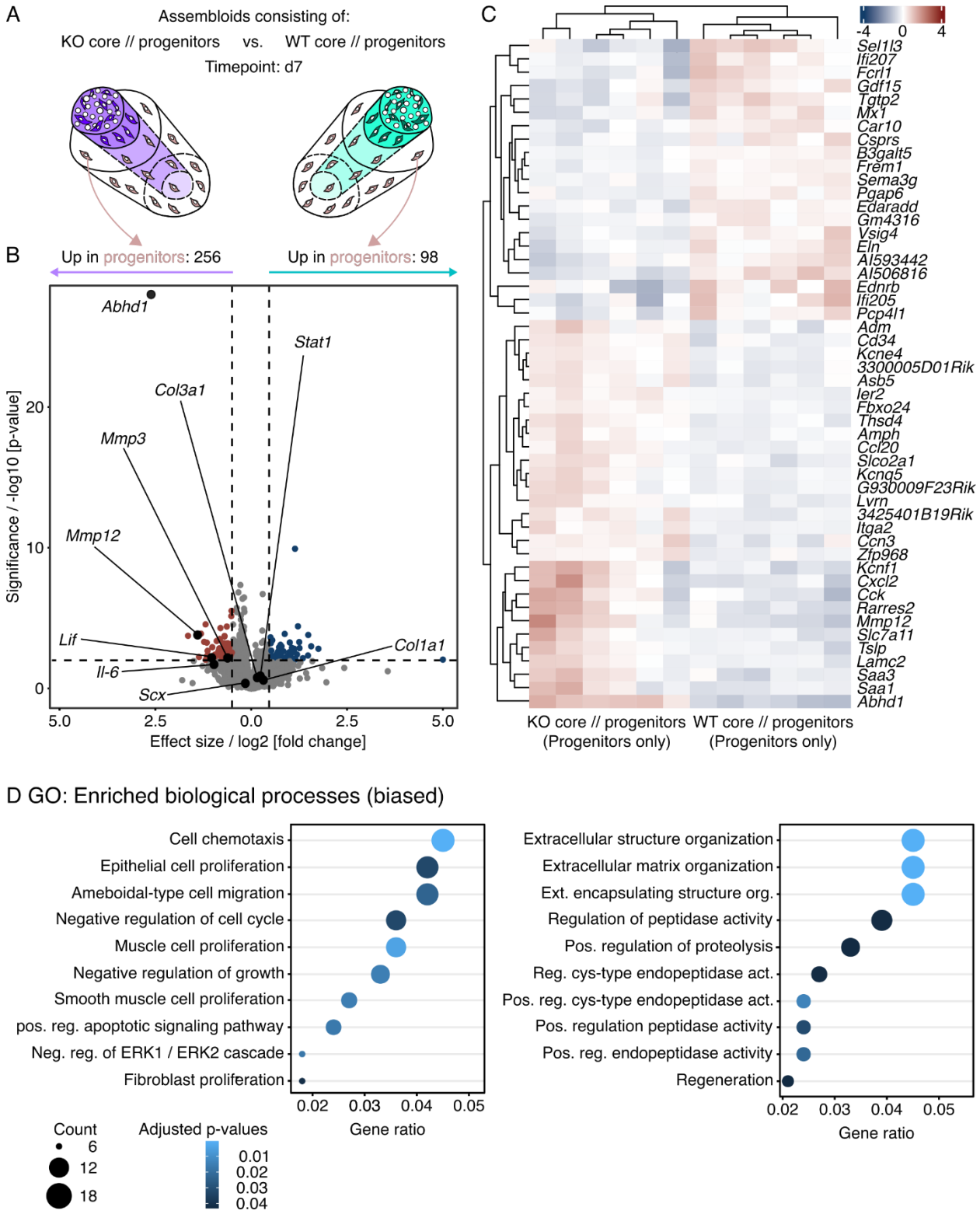

Figure 3: Transcript changes in hydrogel-embedded fibroblast progenitors seeded around an IL-6 knock-out (KO) core explant compared those seeded around a wildtype (WT) core. (A) Illustration of the assembloid combinations compared here (KO core // progenitors vs. WT core // progenitors), the assessed timepoint (d7), and the analyzed compartment (extrinsic fibroblast progenitors only). (B) RNA-seq volcano plot of differentially expressed genes (DEGs). Genes colored in red have a log2 (fold change) > 0.5, a p-value < 0.05, and are considered to be significantly increased in the extrinsic compartment of KO core // progenitor assembloids. Genes colored in blue

have a log2 (fold change) < - 0.5, a p-value < 0.05, and are considered to be significantly increased in the extrinsic compartment of WT core // progenitor assembloids. The log2 and p-value thresholds are represented by the dashed lines. (C) Unsupervised hierarchical clustering of the top 50 differentially expressed genes. Genes are clustered by color with positive (red) or negative (blue) row-scaled z-scores. Columns represent individual samples. N=6. (D) Dotplots depicting a selection of GO annotations significantly enriched (adjusted p-value < 0.05) by the DEGs. The selection was biased by GO biological process annotations enriched in the human dataset (**Figure 1E**). The color of the circles represents their adjusted p-value, the size the number of enriched genes (count), and the x-axis the number of enriched genes in ratio to the total number of genes annotated to the gene set (gene ratio).

When stratifying the respective contribution of transcripts increased and decreased around a KO core to the top 20 enriched GO biological processes and significantly enriched MSigDB mouse hallmarks, we found that IL-6 signaling by the core correlated positively with processes aimed at increasing cellularity and ECM turnover (**Supplementary Figure 4B-D**), which are both hallmarks of tendinopathic tissues and indicators of an activated tissue state.

To verify the transcript-level differences connected to hypercellularity on the tissue-level, we next performed a proliferation and migration analysis in our assembloid model system.

IL-6 signaling by tendon core explants stimulates cell proliferation and Scx$^+$ cell recruitment to the signaling tendon core.

Using the assembloid model, we investigated whether IL-6 signaling could play a causative role in the hypercellularity that is a major hallmark of tendinopathy. Closely mimicking human tendinopathic tendons, we indeed found cellularity-increasing biological processes to be enriched in cell populations around WT compared to those around IL-6 KO tendon core explants. We then assessed whether these IL-6-dependent transcript-level changes would translate to an increased cell density. To do this, we seeded tendon fibroblast progenitor populations isolated from ScxGFP$^+$ mice (co-expressing the tendon-marker Scleraxis (Scx) with a green fluorescent protein) into the hydrogel extrinsic compartment of our assembloids and incorporated either a WT or an IL-6 KO core into the center (**Figure 4A, top panels)**.

Representative fluorescence microscopy images taken after seven days in co-culture confirmed a higher total cell number in WT core // ScxGFP$^+$ progenitor assembloids compared to KO core // ScxGFP$^+$ progenitor assembloids. These cell number differences were not confined to ScxGFP$^+$ progenitors (green) but extended to other populations (blue). In addition, ScxGFP$^+$ progenitors only accumulated around the WT core in WT core // ScxGFP$^+$ progenitor assembloids, presumably either through increased core-directional migration or faster proliferation closer to the core. These observations are consistent with IL-6 being essential to increased cellularity and core (damage)-directed migration in this model.[51]

We went on to confirm these visual impressions using quantitative methods, finding a significantly increased total cell number in assembloids with a WT core compared to those with a KO core (**Table 2 & Figure 4B**). The effect of IL-6 signaling on the proliferation of ScxGFP$^+$ progenitors (**Table 2 & Figure 4C**) was less pronounced compared to that on all populations, but the trend remained the same. To quantify migration, we analyzed the spatial distribution of ScxGFP$^+$ progenitors by calculating the ratio between core-resident and extrinsic ScxGFP$^+$ progenitors (**Table 2 & Figure 4D**). The WT core // ScxGFP$^+$ progenitor assembloids exhibited the highest core-resident to extrinsic ScxGFP$^+$ progenitor ratio and KO core // ScxGFP$^+$

progenitor assembloids had a significantly lower core-resident to extrinsic ScxGFP$^+$ progenitor ratio. The cumulative spatial distribution of ScxGFP$^+$ progenitors (**Table 2 & Figure 4E**) supported these insights.

Condition	**Total cell number norm. to WT (median(IQR))**	**ScxGFP$^+$ cell number norm. to WT (median(IQR))**	**Core / extrinsic ScxGFP$^+$ ratio, norm. to WT (median(IQR))**
WT core // ScxGFP$^+$ progenitors	100(20.1)%	100(19.4)%	100(52.3)%
WT core // ScxGFP$^+$ progenitors + Tocilizumab	87.7(23.5)%	40.7(49.3)%	51.5(14.8)%
KO core // ScxGFP$^+$ progenitors	77.6(14.1)%	62.2(66.1)%	73(40)%
KO core // ScxGFP$^+$ progenitors + IL-6	97.7(22.8)%	89.7(86.1)%	66.1(45.9)%

Table 2: Total cell numbers, ScxGFP$^+$ cell numbers, and the ratios between core-resident and extrinsic ScxGFP$^+$ cells in assembloids. The values were normalized to the WT median and are given as median(IQR).

To further confirm the specific impact of IL-6 signaling on overall cell proliferation and core-directed migration of Scx$^+$ fibroblast progenitors, we desensitized the WT core // progenitor assembloids to IL-6 by neutralizing IL6R with Tocilizumab and attempted to rescue the KO core // progenitor assembloids by adding recombinant IL-6 to compensate for their reduced IL-6 levels (**Figure 4A, bottom panels**). In alignment with the previous results and the hypothesis, IL-6 desensitization decreased the total cell number in trend (**Table 2 & Figure 4B**), the ScxGFP$^+$ cell number significantly (**Table 2 & Figure 4C**,), and the ratio between core-resident and extrinsic ScxGFP$^+$ progenitors significantly as well (**Table 2 & Figure 4D**). The addition of recombinant IL-6 to KO core // progenitor assembloids significantly increased the total cell number and the number of ScxGFP$^+$ cells, rescuing the wildtype phenotype of IL-6 enhanced cell proliferation in the extrinsic compartment. However, core-directed migration was not rescued by recombinant IL-6.

Fully in line with transcript signature changes detected in the extrinsic compartment, these data suggest that IL-6 signaling increases local cellularity in at least two ways. First, IL-6 stimulates both overall and specific ScxGFP$^+$ cell proliferation. Second, IL-6 gradient effects (i.e. IL-6 induced secondary gradients) cause core-directed ScxGFP$^+$ cell migration.

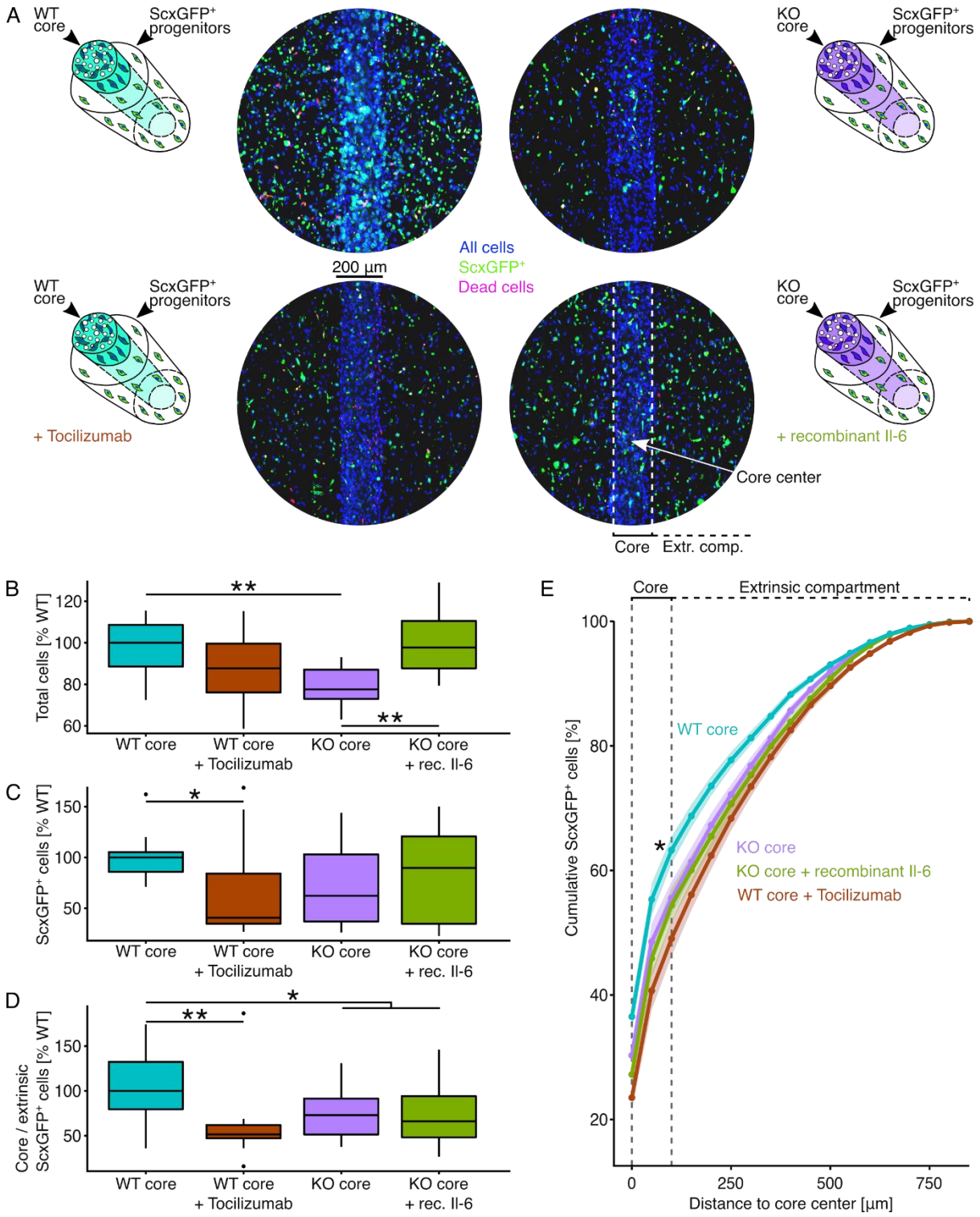

Figure 4: Cell proliferation around and ScxGFP+ fibroblast progenitor recruitment to core explants. (A) Illustrative depictions and representative fluorescence microscopy images of wildtype (WT) core explants surrounded by fibroblast progenitor populations from ScxGFP+ mice cultured with or without Tocilizumab (10 µg/ml), and IL-6 knock-out (KO) explants cultured with or without recombinant IL-6 (25 ng/ml) for 7 days. All cells are colored in blue (NucBlue), ScxGFP+ fibroblast progenitors in green (GFP), and dead cells in red (EthD). (B, C, D) Boxplots depicting the total number of cells, the number of ScxGFP+ cells, and the ratio between core-resident and extrinsic ScxGFP+ cells normalized to the WT median. Each datapoint was calculated from 3 representative fluorescence microscopy images taken from the same sample. The upper and lower hinges

correspond to the first and third quartile (25th and 75th percentile), the middle one to the median, the whiskers extend from the hinges no further than 1.5 times the interquartile range, and the points beyond the whiskers are treated as outliers. (E) Lineplot depicting the cumulative percentage of ScxGFP+ cells depending on their distance from the center line of the core explant. The points and the line represent the mean cumulative percentages and the error bands the standard error of the mean (sem). The dashed line indicates locations inside the core area. N=12. Results of the statistical analysis are indicated as follows: *$p < 0.05$, **$p < 0.01$. The applied statistical test was the Mann-Whitney-Wilcoxon Test.

Disrupting IL-6 signaling reduces Scx$^+$ cell recruitment into a damaged Achilles tendon in vivo.

After clarifying the role of IL-6 in activating progenitor cells in the assembloid model, we sought *in vivo* confirmation that IL-6 signaling enhances overall cell proliferation and migration of Scx$^+$ fibroblast progenitors to tendon damage. To achieve this, we assessed and quantified the presence of Scx$^+$ cells in the Achilles tendons (AT) of WT mice compared to those of IL-6 KO mice seven days after Achilles tenotomy (**Figure 5A**).

Overall, fluorescence microscopy images (**Figure 5B**) revealed a strong presence of Scx$^+$ cells (green) in the neotendon (Nt) formed after tenotomy, which was not present in undamaged hindleg tendons. While similar levels of overall cellularity and presence of Scx$^+$ cells were observed in both WT and IL-6 KO mice (**Table 3** and **Figure 5C & D**), notable differences in Scx$^+$ cell migration patterns were observed (**Table 3 & Figure 5E**). After identifying the locations of Scx$^+$ cells in the tissue sections, we calculated the ratio between Achilles tendon (AT)- and neotendon (Nt)-resident Scx$^+$ cells. Consistent with the *in vitro* experiments, this ratio was significantly increased in the WT compared to the KO Achilles tendon one week after the tenotomy. Again, the cumulative spatial distribution of Scx$^+$ cells supported this finding (**Figure 5F**). Examining other progenitor markers (CD146 and TPPP3, **Supplementary Figure 5A-E**) we found no differences in the total number of cells expressing them, their relative percentages, or their recruitment patterns. Our finding that IL-6 KO mice display altered recruitment of Scx$^+$ cells to sites of damage plausibly explains earlier reports of an impaired tendon healing response in IL-6 knock-out mice.[54] Our data suggest that loss of IL-6 activation of Scx$^+$ fibroblast progenitors could delay *in vivo* healing after injury.

Condition	**Total cell number (median(IQR))**	**Scx$^+$ percentage (median(IQR))**	**AT / Nt Scx$^+$ ratio (median(IQR))**
IL-6 WT: Achilles tenotomy	1433(287)	35(25.2)	3(8.3)
IL-6 KO: Achilles tenotomy	1471(163)$^{n.s.}$	38.1(45.9)$^{n.s.}$	2(0.4)*

Table 3: Total cell number, Scx$^+$ percentage, and the ratios between Achilles tendon (AT)- and neotendon (Nt)-resident Scx$^+$ cells in WT and KO mice after Achilles tenotomy. The values were determined from sections isolated seven days after the Achilles tenotomy and are given as median(IQR). Statistically significant differences of the KO compared to the WT are indicated as follows: *$p < 0.05$, $^{n.s.}p > 0.05$.

Building upon the evidence that IL-6 potentiates tendon progenitor activation and migration to damage, we sought to clarify the nature of interactions between these recruited repair cells and the damaged tissue. Here we again turned to our assembloid model system to dissect effects of fibroblast progenitors on the core explant *in vitro*.

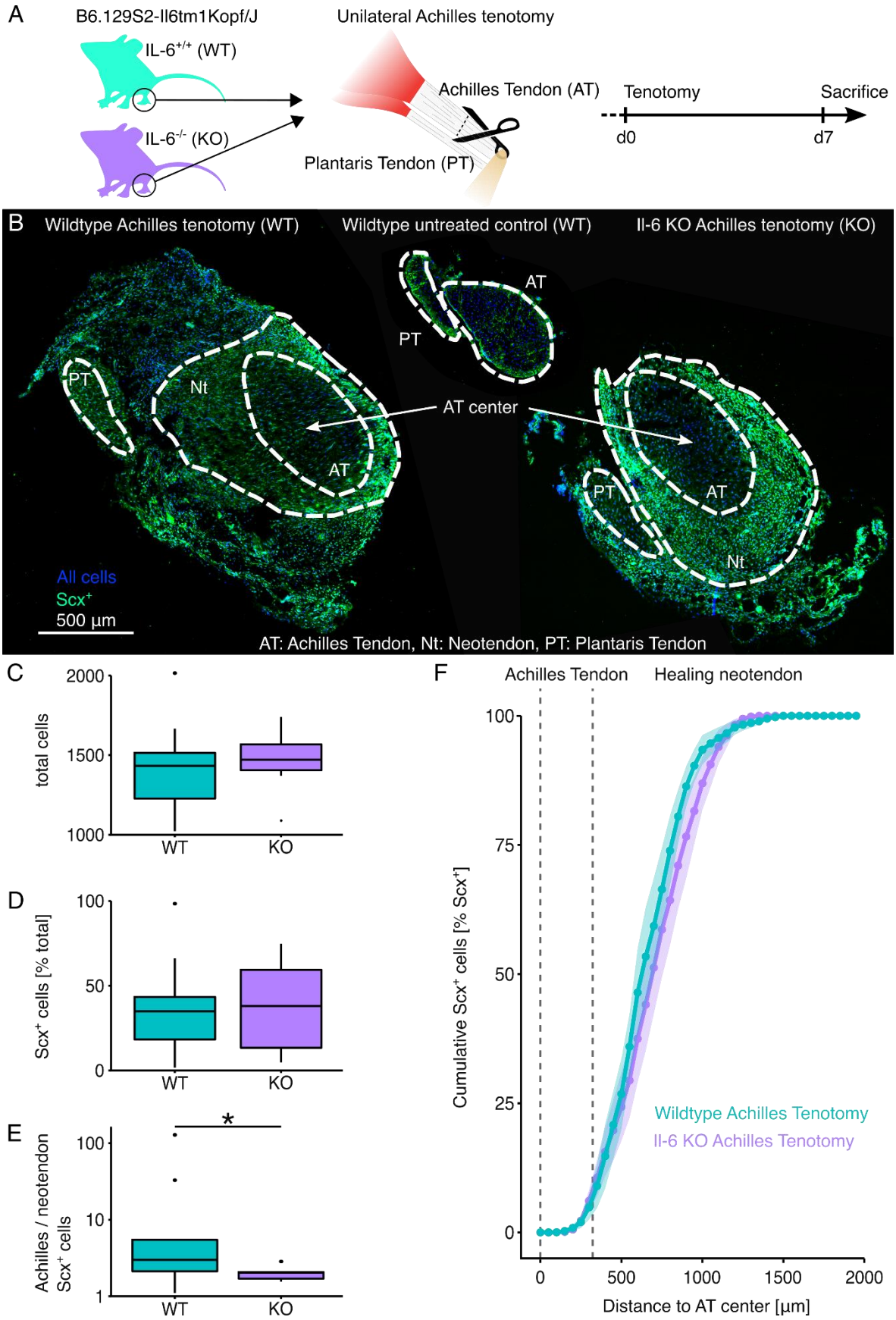
A
B6.129S2-Il6tm1Kopf/J
IL-6+/+ (WT)
IL-6-/- (KO)
Unilateral Achilles tenotomy
Achilles Tendon (AT)
Plantaris Tendon (PT)
Tenotomy
Sacrifice
d0
d7
B
Wildtype Achilles tenotomy (WT)
Wildtype untreated control (WT)
Il-6 KO Achilles tenotomy (KO)
PT
Nt
AT
AT center
All cells
Scx+
500 µm
AT: Achilles Tendon, Nt: Neotendon, PT: Plantaris Tendon
C
total cells
2000
1500
1000
WT
KO
D
Scx+ cells [% total]
100
50
0
WT
KO
E
Achilles / neotendon Scx+ cells
100
10
1
*
WT
KO
F
Achilles Tendon
Healing neotendon
Cumulative Scx+ cells [% Scx+]
100
75
50
25
0
Wildtype Achilles Tenotomy
Il-6 KO Achilles Tenotomy
0
500
1000
1500
2000
Distance to AT center [µm]

Figure 5: Cell proliferation around and Scx+ fibroblast progenitor recruitment to damaged mouse Achilles tendons. (A) Illustrative depiction of the experimental setup and the time schedule. (B) Representative fluorescence microscopy images of mouse hindleg sections from wildtype (WT) Achilles tendons that underwent tenotomy (left), the contralateral untreated control (middle), as well as sections from IL-6 knock-out (KO) Achilles tendons that underwent tenotomy (right). (C) Total number of cells stained with NucBlue. (D) Number of Scx+ cells. (E) Ratio between core-resident and extrinsic Scx+ cells depicted on a logarithmic y-axis. N=7. The upper and lower hinges correspond to the first and third quartile (25th and 75th percentile), the middle one to the median, the whiskers extend from the hinges no further than 1.5 times the interquartile range, and the points beyond the whiskers are treated as outliers. (F) Lineplot depicting the cumulative percentage of Scx+ cells depending on their distance from the Achilles tendon center. The points and the line represent the mean cumulative percentages and their error bands the standard error of the mean (sem). The dashed line indicates locations inside the Achilles tendon stump. Results of the statistical analysis are indicated as follows: *$p < 0.05$. The applied statistical tests was the Mann-Whitney-Wilcoxon Test.

Activated, proliferating, and recruited extrinsic fibroblast progenitors promote tendinopathy hallmarks in tendon core explants.

Our data presented in previous sections directly connect IL-6 signaling to the activation of Scx^+ tendon progenitor cells, as well as their proliferation and directed migration to damage. We then asked whether these activated fibroblast progenitors might be capable of driving disease-relevant tissue processes. To assess this, we first looked at transcriptional changes induced in core explants when fibroblast progenitors were present in the artificial extrinsic compartment, compared to explants cultured in an initially cell-free hydrogel (**Figure 6A**).

Exposing WT core explants to fibroblast progenitors (WT core // progenitors) for seven days increased 446 transcripts, decreased 217 transcripts, and left 19'694 transcripts unchanged (**Figure 6B & C**). In line with the previous paragraphs reporting fibroblast progenitor migration, some of the increased transcripts (i.e. Scx and Sox9) indicated an enrichment of Scx^+ and / or $Sox9^+$ fibroblast progenitors in the WT core explants of WT core // progenitor assembloids. Similarly, GSEA on the full MSigDB cell type signature gene sets proposed an amplified contribution of fibroblasts, fibroblast-like, and progenitor cells to the emerging assembloid phenotype (**Supplementary Figure 6B**). *In vivo*, extrinsic (i.e. paratenon-derived) fibroblast progenitors differentially express selected genes compared to tendon core (i.e. tendon proper-derived) fibroblast progenitors.[66] The GO gene sets annotated with these differentially expressed genes (DEGs) overlap with those enriched by DEGs between WT core // progenitor and WT core // cell-free assembloids (**Supplementary Figure 7A-D**). This could mean that the core explants exposed to extrinsic fibroblast progenitors change into more paratenon-like tissue and again highlights the contribution of extrinsic fibroblast progenitor migration and accumulation to assembloid behavior.

To compare this phenotype to human tendinopathic tendons, we looked for ECM turnover-related transcripts that were enriched in human tendinopathic tendons. Indeed, transcripts for *Col3a1*, *Col1a1*, *Mmp13*, *Mmp3*, and *Mmp9* were increased in core explants co-cultured with fibroblast progenitors (**Figure 6A & Table 4**). When combined through ORA, many of the top 30 biological processes enriched by significantly changed transcripts (adjusted p-value < 0.01) were also enriched in human tendinopathic tendons (**Supplementary Figure 6C**). The curated list presented here (**Figure 6D**) pinpoints significantly enriched processes likely to be involved in tendinopathic hallmarks such as ECM turnover & tissue development, hypoxia & glucose metabolism, and hypercellularity. Furthermore, many signaling pathways dysregulated in human tendinopathy were significantly enriched by differentially expressed genes in core explants co-

cultured with fibroblast progenitors as well, including Wnt / β-catenin and IL-6 (**Figure 1 & Figure 6D)**.

Transcript	Effect size	P-value
Col3a1	1.1	8.4e-11
Col1a1	0.8	0.06
Mmp13	0.91	1.2e-06
Mmp3	0.64	0.0006
Mmp9	1.45	0.019
Scx	0.98	0.00006
Sox9	0.6	0.001

Table 4: Effect sizes and p-values for selected transcripts. The data describes differences in transcripts between the core explants from WT core // progenitors and those from WT core // cell-free assembloids.

Overall, it appears that extrinsic fibroblast progenitors are sufficient to invoke several tendinopathic hallmarks in tendon core explants and accelerated catabolic matrix turnover in particular. We have previously reported an increase of IL-6 in the supernatant of WT core // progenitor assembloids that correlated with an increased catabolic breakdown of the core.[51] The insights gained here connect this catabolic breakdown to genes sets involved in ECM remodeling. Another set of previously published experiments suggests that the ERK1/2 signaling cascade enriched here favors tissue breakdown as well.[67,68]

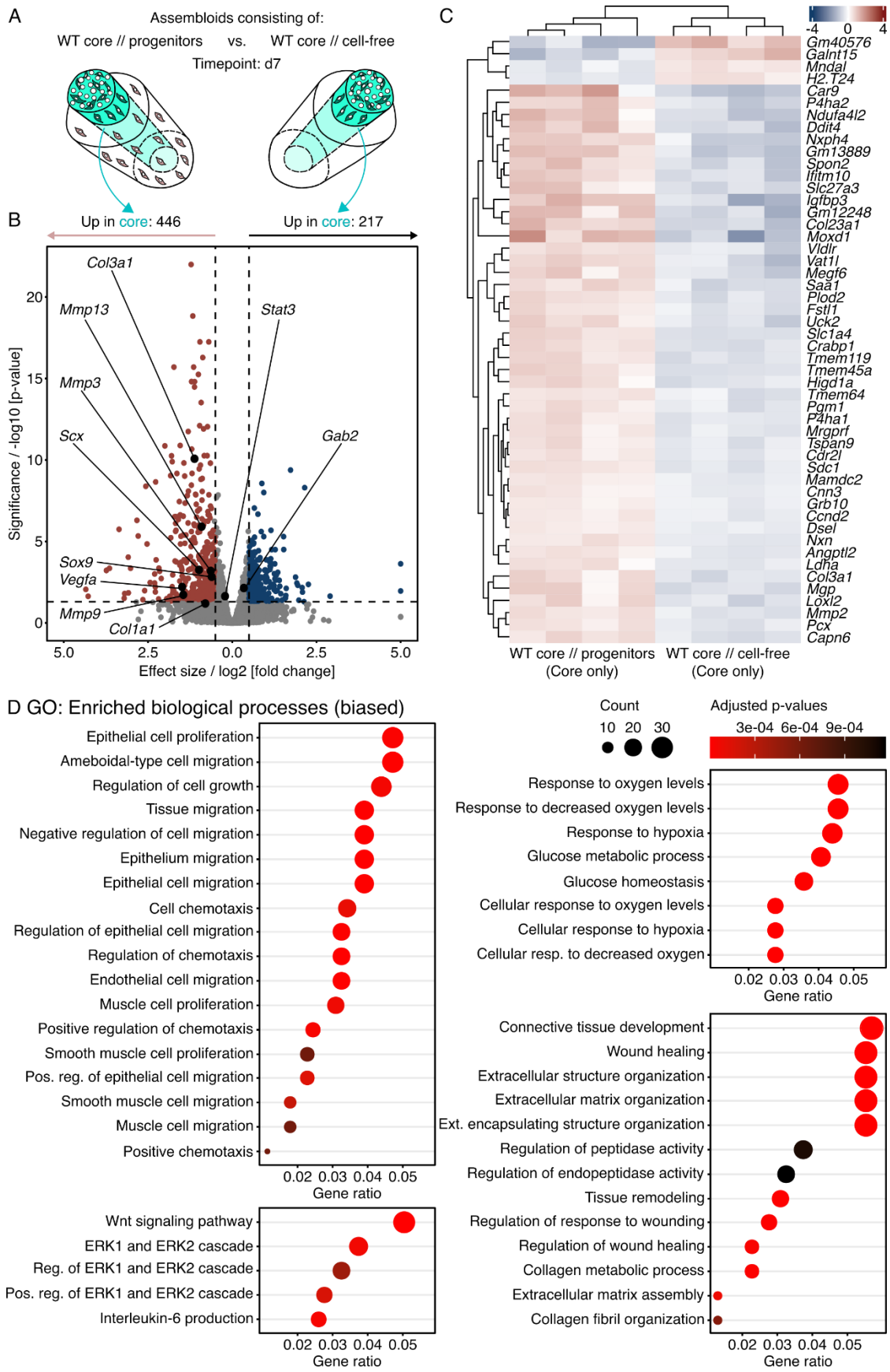
A
Assembloids consisting of:
WT core // progenitors vs. WT core // cell-free
Timepoint: d7
B
Up in core: 446
Up in core: 217
Col3a1
Mmp13
Mmp3
Scx
Sox9
Vegfa
Mmp9
Col1a1
Stat3
Gab2
Significance / -log10 [p-value]
Effect size / log2 [fold change]
C
Gm40576
Galnt15
Mndal
H2.T24
Car9
P4ha2
Ndufa4l2
Ddit4
Nxph4
Gm13889
Spon2
Ifitm10
Slc27a3
Igfbp3
Gm12248
Col23a1
Moxd1
Vldlr
Vat1l
Megf6
Saa1
Plod2
Fstl1
Uck2
Slc1a4
Crabp1
Tmem119
Tmem45a
Higd1a
Tmem64
Pgm1
P4ha1
Mrgprf
Tspan9
Cdr2l
Sdc1
Mamdc2
Cnn3
Grb10
Ccnd2
Dsel
Nxn
Angptl2
Ldha
Col3a1
Mgp
Loxl2
Mmp2
Pcx
Capn6
WT core // progenitors (Core only)
WT core // cell-free (Core only)
D GO: Enriched biological processes (biased)
Count
Adjusted p-values
Epithelial cell proliferation
Ameboidal-type cell migration
Regulation of cell growth
Tissue migration
Negative regulation of cell migration
Epithelium migration
Epithelial cell migration
Cell chemotaxis
Regulation of epithelial cell migration
Regulation of chemotaxis
Endothelial cell migration
Muscle cell proliferation
Positive regulation of chemotaxis
Smooth muscle cell proliferation
Pos. reg. of epithelial cell migration
Smooth muscle cell migration
Muscle cell migration
Positive chemotaxis
Gene ratio
Response to oxygen levels
Response to decreased oxygen levels
Response to hypoxia
Glucose metabolic process
Glucose homeostasis
Cellular response to oxygen levels
Cellular response to hypoxia
Cellular resp. to decreased oxygen
Wnt signaling pathway
ERK1 and ERK2 cascade
Reg. of ERK1 and ERK2 cascade
Pos. reg. of ERK1 and ERK2 cascade
Interleukin-6 production
Connective tissue development
Wound healing
Extracellular structure organization
Extracellular matrix organization
Ext. encapsulating structure organization
Regulation of peptidase activity
Regulation of endopeptidase activity
Tissue remodeling
Regulation of response to wounding
Regulation of wound healing
Collagen metabolic process
Extracellular matrix assembly
Collagen fibril organization

Figure 6: Transcript analysis of differentially regulated genes and pathways in wildtype (WT) core explants surrounded by a hydrogel seeded with fibroblast progenitors compared to a WT core surrounded by a cell-free hydrogel. (A) Illustration depicting the assembloid combinations compared here (WT core // progenitors vs. WT core // cell-free), the assessed timepoint (d7), and the analyzed compartment (core only). (B) RNA-seq volcano plot of differentially expressed genes (DEGs). Genes colored in red have a log2 (fold change) > 0.5, an adjusted p-value < 0.05, and are considered to be significantly increased in the core of WT core // progenitor assembloids. Genes colored in blue have a log2 (fold change) < - 0.5, an adjusted p-value < 0.05, and are considered to be significantly increased in in the core of WT core // cell-free assembloids. The log2 and p-value thresholds are represented by the dashed lines. (C) Unsupervised hierarchical clustering of the top 50 differentially expressed genes. Genes are clustered by color with positive (red) or negative (blue) row-scaled z-scores. Columns represent individual samples. N=4. (D) Dotplots depicting a selection of GO annotations significantly enriched (adjusted p-value < 0.05) by the DEGs. The selection was biased by GO biological processes and GSEA hallmark annotations enriched in the human dataset (**Figure 1C & E**). The color of the circles represents their adjusted p-value, the size the number of enriched genes (count), and the x-axis the number of enriched genes in ratio to the total number of genes annotated to the gene set (gene ratio).

Disrupting IL-6 signaling in core explants diminishes emergence of tendinopathic hallmarks.

So far, our results have shown that IL-6 signaling enhances proliferation and migration of fibroblast progenitors towards the tendon core and that the presence of fibroblast progenitors invokes tendinopathy-like changes in the tendon core. Consequently, the last step was to see whether an IL-6 knock-out not only prevents the fibroblast progenitor migration and proliferation, but also reduces fibroblast progenitor-invoked tendinopathic hallmarks in the core. To assess this, we again studied assembloids containing an IL-6 KO core, but this time focused on biological processes emerging in the core by leveraging bulk RNA-sequencing (**Figure 7A**).
On the transcript level, we found 276 upregulated, 192 downregulated, and 20'204 unchanged genes in the core of KO core // progenitor assembloids compared to that of WT core // progenitor assembloids (**Figure 7B & C**). To see whether an IL-6 knock-out would partially reverse fibroblast progenitor-invoked hallmarks, we matched the list of differentially expressed genes (p-value < 0.01) to the signatures in the GO database and then compared the surfacing enriched biological processes with those enriched by differentially expressed genes between the core of a WT core // progenitor assembloid and a WT core // cell-free assembloid. The largest overlap lay in the signaling pathways (Wnt, ERK1/2, and IL-6), where 5/5 signatures for biological processes remained similarly enriched (**Figure 7E**). We found slightly fewer overlapping signatures connected to ECM turnover (6/14) and cellularity (6 /18) while there seemed to be a disconnect in hypoxia & glucose metabolism (2/8). Overall, about a third of all signatures enriched by the presence of fibroblast progenitors where also enriched by the IL-6 KO (**Figure 7E**). Regarding the respective contribution of increased and decreased transcripts to the enriched GO biological processes and molecular functions, it seems that the IL-6 KO correlates positively with processes aimed at decreasing cellularity and ECM turnover in the core (**Supplementary Figure 8**), which could mean that IL-6 signaling indeed contributes to these tendinopathy hallmarks on the gene level.

As we have already demonstrated the tissue-level effects of IL-6 signaling on cellularity (**Figure 4**), we next wanted to examine the tissue-level consequences of changed transcript signatures for ECM turnover on core biomechanics. To do so, we measured the assembloid's linear elastic modulus as an indicator for their ability to resist longitudinal tension, which is one of the main functions of adult tendons (**Figure 7F**). In WT core // progenitor assembloids, the linear elastic

modulus decreased the most between the initial clamping of the core explant and 21 days of co-culture (light blue). The linear elastic modulus of assembloids containing a KO core (violet) or a WT core explant devitalized through multiple freeze-thaw cycles (black) decreased as well, but not as fast or as strongly. In connection with the bulk RNA-seq data, the changes in the assembloid's ability to resists tension suggest that IL-6 signaling accelerates (catabolic) ECM turnover.

Normally, it would be hard to predict the effect of an accelerated catabolic ECM turnover *in vitro* on wound healing *in vivo* since both ECM degradation and synthesis are required to replace damaged tissue structures. However, previous studies have already reported a delayed wound healing response in IL-6 KO mice and our experiments here suggest that the decelerated catabolic ECM turnover could be responsible for this.[54]

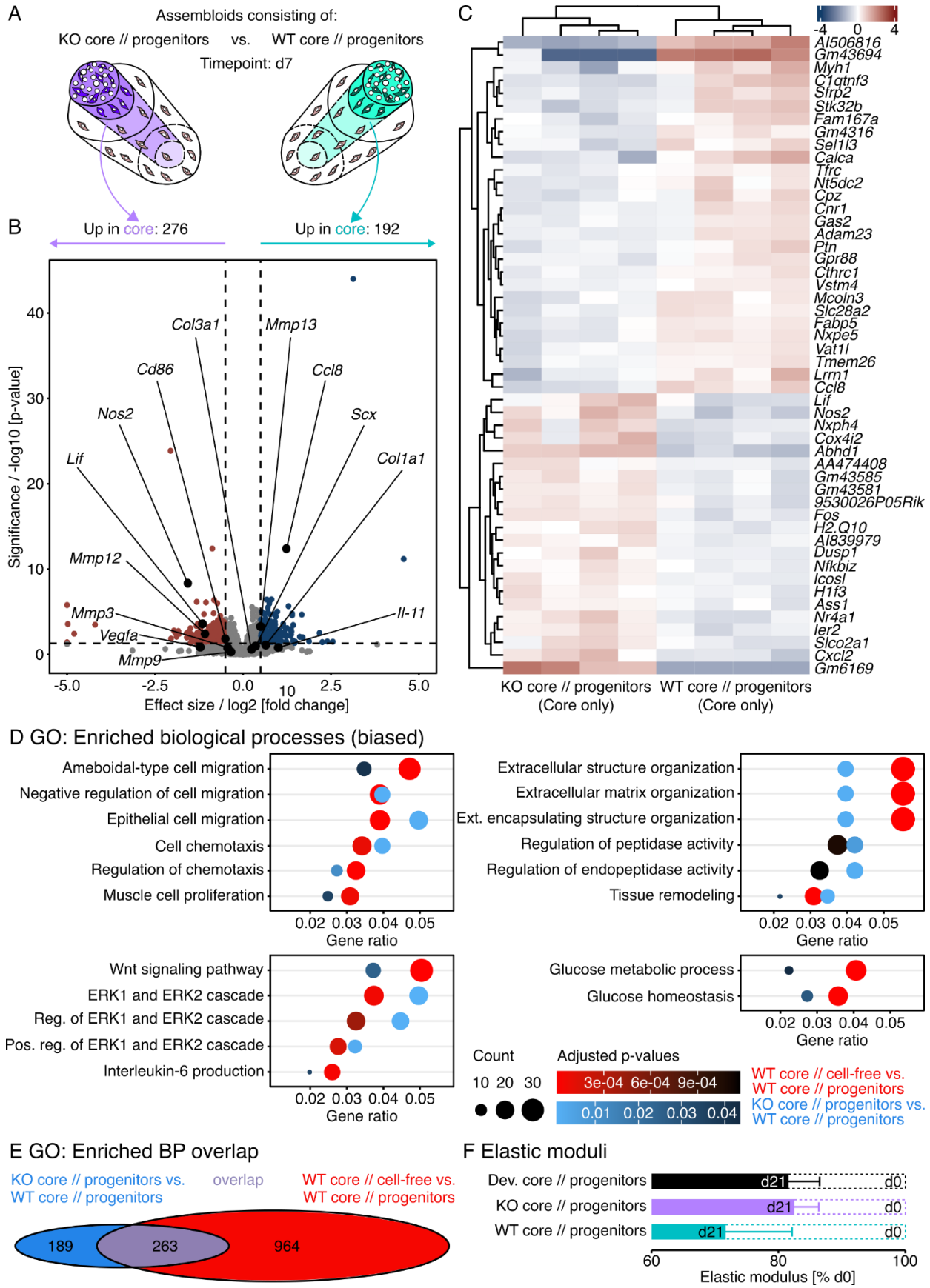
A
Assembloids consisting of:
KO core // progenitors vs. WT core // progenitors
Timepoint: d7
B
Up in core: 276
Up in core: 192
Significance / -log10 [p-value]
Effect size / log2 [fold change]
Col3a1
Mmp13
Cd86
Ccl8
Nos2
Scx
Lif
Col1a1
Mmp12
Mmp3
Il-11
Vegfa
Mmp9
C
Al506816
Gm43694
Myh1
C1qtnf3
Sfrp2
Stk32b
Fam167a
Gm4316
Sel1l3
Calca
Tfrc
Nt5dc2
Cpz
Cnr1
Gas2
Adam23
Ptn
Gpr88
Cthrc1
Vstm4
Mcoln3
Slc28a2
Fabp5
Nxpe5
Vat1l
Tmem26
Lrrn1
Ccl8
Lif
Nos2
Nxph4
Cox4i2
Abhd1
AA474408
Gm43585
Gm43581
9530026P05Rik
Fos
H2.Q10
Al839979
Dusp1
Nfkbiz
Icosl
H1f3
Ass1
Nr4a1
Ier2
Slco2a1
Cxcl2
Gm6169
KO core // progenitors (Core only)
WT core // progenitors (Core only)
D GO: Enriched biological processes (biased)
Ameboidal-type cell migration
Negative regulation of cell migration
Epithelial cell migration
Cell chemotaxis
Regulation of chemotaxis
Muscle cell proliferation
Extracellular structure organization
Extracellular matrix organization
Ext. encapsulating structure organization
Regulation of peptidase activity
Regulation of endopeptidase activity
Tissue remodeling
Wnt signaling pathway
ERK1 and ERK2 cascade
Reg. of ERK1 and ERK2 cascade
Pos. reg. of ERK1 and ERK2 cascade
Interleukin-6 production
Glucose metabolic process
Glucose homeostasis
Gene ratio
Count
Adjusted p-values
WT core // cell-free vs. WT core // progenitors
KO core // progenitors vs. WT core // progenitors
E GO: Enriched BP overlap
KO core // progenitors vs. WT core // progenitors
overlap
WT core // cell-free vs. WT core // progenitors
189
263
964
F Elastic moduli
Dev. core // progenitors
KO core // progenitors
WT core // progenitors
d21
d0
Elastic modulus [% d0]

Figure 7: Transcript analysis of differentially regulated genes and pathways in IL-6 knock-out (KO) core explants surrounded by a hydrogel seeded with fibroblast progenitors compared to a wildtype (WT) core surrounded by fibroblast progenitors. (A) Illustration depicting the assembloid combinations compared here (KO core // progenitors vs. WT core // progenitors), the assessed timepoint (d7), and the analyzed compartment (core only). (B) RNA-seq volcano plot of differentially expressed genes (DEGs). Genes colored in red have a log2 (fold change) > 0.5, a p-value < 0.05, and are considered to be significantly increased in the core of KO core // progenitor assembloids. Genes colored in blue have a log2 (fold change) < - 0.5, a p-value < 0.05, and are considered to be significantly increased in the core of WT core // progenitor assembloids. The log2 and p-value thresholds are represented by the dashed lines. (C) Unsupervised hierarchical clustering of the top 50 differentially expressed genes. Genes are clustered by color with positive (red) or negative (blue) row-scaled z-scores. Columns represent individual samples. N=4. (D) Dotplots depicting a selection of GO annotations significantly enriched (adjusted p-value < 0.05) by the DEGs in both the WT core // cell-free vs. WT core // progenitor assembloid comparison (red to black gradient) and the KO core // progenitor vs. WT core // progenitor assembloid comparison (light blue to black gradient). The selection was biased by enriched GO biological process and GSEA hallmark annotations in the human dataset (**Figure 1C & E**). The color gradient of the circles represents their adjusted p-value, the size the number of enriched genes (count), and the x-axis the number of enriched genes in ratio to the total number of genes annotated to the gene set (gene ratio). (E) Venn-Diagramm depicting the number and the overlap (violet) of significantly enriched GO annotations for biological processes between the WT core // cell-free vs. WT core // progenitor assembloid comparison (red) and the KO core // progenitor vs. WT core // progenitor assembloid comparison (blue). (F) Linear elastic moduli of devitalized (Dev.), IL-6 knock-out (KO), and wildtype (WT) core explants surrounded by hydrogel-embedded fibroblast progenitor populations at day 21 normalized to day 0. N=8. The data are displayed as barplots with mean ± standard error of the mean (sem). The applied statistical test was the Mann-Whitney-Wilcoxon Test and yielded no significant differences.

DISCUSSION

Interleukin-6 (IL-6) is an attractive translational research target. Signaling cascades related to IL-6 are upregulated in tendon tissues after exercise, acute tissue damage, and in chronic tendon disease.[55,57,69] Little is currently understood of the precise role that IL-6 plays in these processes.[70] The goal of the present work was to clarify the role of IL-6 signaling in the tendon tissue's response to damage, with a particular focus on inter-compartmental crosstalk between the damaged tendon core and extrinsic fibroblast progenitor populations targeted by it.

We first reanalyzed existing microarray data of tendinopathic tendons to verify a hypothesized (dys)functional role of IL-6 that seems to run partially via JAK/STAT pathway enriched by increased transcripts. The JAK/STAT pathway interweaves with ERK1/2 downstream, which fits with recent data from our lab showing that ERK inhibition alone can prevent tendon matrix deterioration while reducing the secretion of IL-11, another member of the IL-6 cytokine family that was also upregulated in the tendinopathic tendons analyzed here.[67,68] More generally, overactivation of JAK/STAT/ERK has been associated with auto-immune arthritis.[34,35]
While analysis of human samples indicated the expression of *IL-6* and *ADAM10* (known to transform membrane-bound Il6R into soluble Il6R) to be upregulated in tendinopathic tendons, the expression of *Il6R* itself was downregulated. We speculate that this points towards increased trans-signaling aimed at stromal cells unable to express *Il6R*, in this tendinopathic context particularly stromal fibroblasts, progenitors, and satellite cell-like populations as reported by the cell type signatures.[71] This theory is supported by enriched GO terms relating to increased ECM turnover and wound healing, both processes supposedly powered by fibroblast progenitors.[72,73] Most of the remaining top 20 enriched GO terms pointed towards increased cell proliferation, potentially increasing the leverage of the proliferating fibroblast progenitors.

While beneficial in controlled dosages during normal wound healing, both excessive hypercellularity and imbalanced matrix turnover are also hallmarks of tendinopathy. However, deciphering their direct connections to IL-6 *in vivo* is rather challenging due to unclear IL-6 sources and concentration gradients. For the second part of this work, we therefore turned to tendon assembloids: hybrid explant // hydrogel models of core tendon damage and repair that were recently developed in our lab and which identified an underloaded core explant as a potentially biologically relevant source of IL-6.[51] The simultaneously increased and imbalanced matrix tissue turnover perpetuated by the crosstalk between the core and an extrinsic fibroblast progenitor population seemed to put the system into a prime position to decipher the connections between IL-6, hypercellularity, and (catabolic) matrix turnover.

Replacing the wildtype core explant with an IL-6 KO core explant in our assembloids was sufficient to reduce the expression of genes in gene sets related to matrix turnover, proteolysis, cell proliferation, and cell migration in the extrinsic fibroblast progenitor population. We confirmed the IL-6-induced gene-level differences regarding cell migration by exploiting trackable ScxGFP$^+$ progenitors and demonstrated effective manipulation of both recruitment and proliferation of ScxGFP$^+$ cells through IL-6. We did so by using the IL-6 inhibitor Tocilizumab to desensitize resident cell populations to IL-6 and recombinant IL-6 to replace the IL-6 not secreted by an IL-6 KO core. Recombinant IL-6 rescuing proliferation but not migration of ScxGFP$^+$ cells highlights the necessity of an IL-6 gradient and / or the establishment of a secondary cytokine gradient (e.g. TGF-β) by IL-6.[19] Alternatively, IL-6 has also been described as an energy allocator

in other musculoskeletal tissues and could in this function be accelerating a diverse range of processes (i.e. migration) by increasing the baseline cell metabolism.[29] Fittingly, the extrinsic cell populations around an IL-6 KO core upregulated biological processes related to oxidative stress and hypoxia, which indicates a disrupted energy allocation. Since we found similar biological processes to be enriched in human tendinopathic tendons, future studies should more closely examine the role of hypoxic signaling in the pathogenesis of tendinopathy.

To transfer these insights from our *in vitro* experiments to an *in vivo* setup, we used an Achilles tenotomy model of the *in vivo* tendon damage response. These *in vivo* results supported our *in vitro* finding that IL-6 activates Scx$^+$ fibroblast progenitor cells,[74] which then either migrate into or proliferate faster in the damaged and unloaded Achilles tendon stump. Consequently, one could expect a decelerated healing response upon acute injury in IL-6 KO mice. Indeed, previous studies with mice subjected to a patellar punch procedure reported reduced mechanical properties in the healing patellar tendon of IL-6 KO mice compared to the WT.[54] However, we are cautious in interpreting these *in vivo* results, mainly because the Achilles tenotomy model system represents an acute rather than a chronic tendon lesion.[49,75] Also, although the detected difference was statistically significant, simplifying assumptions were applied to interpreting the observed migration patterns and available Scx antibodies are known to be plagued by considerable background noise.[54] Furthermore, one can currently only speculate on the spatial distribution of IL-6 and its tissue gradients that emerge *in vivo* as well as the resulting patterns of inward progenitor cell migration.[18,69]

Since the migrating Scx$^+$ progenitors were apparently targeting the damaged core tissue (likely to support the limited intrinsic regenerative potential of the explanted tendon core secreting IL-6 in the first place)[56], the next set of experiments we conducted in this work focused on the effects of the activated and recruited fibroblast progenitors on the tendon core.

According to existing literature, in particular Scx$^+$ fibroblast progenitors are increasingly present in *in vivo* murine adult tendon lesions[18,19] and depleting them alternately improves or impairs adult tendon healing depending on the timepoint of depletion.[74,76,77] One underlying reason could be that adult, Scx$^+$ fibroblast progenitor cells hold a bi-fated potential that enables a cartilage-like differentiation when exposed to mechanical compression or tensile unloading.[12,78] Our *in vitro* assembloid model captured these behaviors as well with increased Scx / Sox9 transcripts and enriched gene sets indicating a stronger presence of fibroblast progenitors alongside cartilage development in a core surrounded by (migrating) fibroblast progenitors compared to one embedded in a cell-free hydrogel. Besides, genes differentially expressed in a core explant surrounded by fibroblast progenitors enriched gene sets related to hypercellularity, ERK1/2 signaling, oxygen / glucose metabolism, and ECM turnover. Most of these processes were reduced in an IL-6 KO core, speculatively because of the reduced presence of extrinsic fibroblast progenitors resulting from the reduced migration and proliferation. On the tissue-level, we also found signs for a decreased catabolic matrix turnover in the more stable mechanical properties of IL-6 KO core explants, a process likely linked to ERK1/2 signaling.[67]

In summary, our data consistently point to IL-6 signaling targeting stromal (progenitor) cells being upregulated in chronic human tendon lesions in a manner that directly leads to fibroblast progenitor recruitment and proliferation as well as aberrant matrix turnover. This activity contributes to typical hallmarks of tendinopathy including hypercellularity and loss of biomechanical tissue integrity. Our hybrid explant // hydrogel assembloid model suggests that

IL-6 is necessary for the recruitment of Scx^+ progenitors in a role analogous to satellite cell recruitment in muscle tissue.[23,27] Overall, IL-6 in tendon seems so assume the role of a general tissue activator and energy allocator to initiate and power recovery of acute tendon lesions, but may also aggravate hallmarks of chronic tendon lesions through the same action.

EXPERIMENTAL SECTION

Human microarray data analysis

We reanalyzed a microarray dataset (GEO: GSE26051) from 2011 with contemporary methods (principal component analysis, volcano plots, heatmaps, GSEA, and ORA), focusing on the Il-6 signaling cascade. All steps from downloading the dataset to the differential expression computation were conducted in RStudio ("Prairie Trillium", 9f796939, 2022-02-16) running R version 4.1.2. Overall, we closely followed the steps described here: https://sbc.shef.ac.uk/geo_tutorial/tutorial.nb.html (last visited: 02.05.22). First, we $\log_2$-transformed the expression values and checked their distribution with boxplots. Since the original dataset was gathered from a wide variety of anatomical locations and differently aged patients (**Supplementary Table 1**), we started with a principal-component analysis to filter-out outliers. We excluded the samples GSM639748 (Brachialis), GSM639761 (ECRB), GSM639751 (Flexor-Pronator), GSM639756 (Flexor-Pronator), GSM639765 (ECRL), GSM639766 (Subscapularis), GSM639755 (Subscapularis), GSM639780 (Supraspinatus), GSM639782 (Supraspinatus), GSM639788 (ECRB), GSM639773 (Patella), GSM639786 (Supraspinatus), and GSM639775 (Supraspinatus).
To improve the power to detect differentially expressed genes, we filtered-out genes with very low expression. We considered 50% of genes to not be expressed and therefore used the median expression as the cut-off. In addition, we only kept genes expressed in more than 2 samples for further analysis and calculated the average of replicated probes. Afterwards, we applied the empirical Bayes' step to receive the differential expression values and p-values. We plotted the differentially expressed genes (DEGs) as a volcano plot and annotated IL-6 signaling-related genes, other cytokines of the IL-6 family, their respective receptors, and genes involved in matrix turnover. Here, we considered genes with a p-value < 0.05 to be differentially expressed. In addition, we plotted the row scaled z-scores of a selection of the annotated genes in a heatmap.

To produce the GO annotations, we fed the list of IDs from differentially expressed genes into the enrichGO function from the clusterProfiler package (version 3.0.4, https://www.rdocumentation.org/packages/clusterProfiler/versions/3.0.4/topics/enrichGO, last visited: 31.10.22) using the org.Hs.eg.db as reference and the Benjamini-Hochberg method to calculate the false discovery rate / adjust the p-values. To visualize the data, we used the emapplot function and the dotplot function from the enrichPlot package (https://rdrr.io/bioc/enrichplot/, last visited: 31.10.22). We also looked at the increased (logFC > 0) and decreased (logFC < 0) transcripts in isolation to estimate their contribution to the enrichment and give it directionality. For the gene set enrichment analysis (GSEA) performed in RStudio with clusterProfiler, we used the human hallmark and the cell type signature gene set annotations from the molecular signature database (MSigDB, https://www.gsea-msigdb.org/gsea/msigdb/, last visited: 31.10.22) after ranking the genes according to their p-value. We used the following input parameters: pvalueCutoff = 1.00, minGSSize = 15, maxGSSize = 500, and eps=0. Lastly, we used the gseaplot and dotplot functions from the enrichPlot package to plot the data and the sign of the enrichment score / NES to estimate the directionality.

Mouse tissue harvest

We extracted tail tendon core explants and Achilles tendons from 12- to 15-week-old male and female Tgf(Scx-GFP)1Stzr and B6.129S2-Il6tm1Kopf/J Il-6$^{-/-}$ mice (knock-out: KO, wildtype: WT)

as described previously (**Figure 2B & C**).[51] All experiments were approved by the responsible authorities (Canton Zurich license number ZH104-18 & ZH058-21).
We isolated the core explants from the tail and only kept those with a mean diameter between 100 and 150 µm in standard culture medium (DMEM/F12 GlutaMAX with 10% fetal bovine serum, 1% Penicillin / Streptomycin, 1% Amphotericin, 200 µM L-Ascorbic Acid) until clamping them. Meanwhile, we separated the Achilles tendon from the calcaneus and the calf muscle using a scalpel and washed them with PBS before starting the digestion process (Standard culture medium without L-Ascorbic Acid but 2 mg/ml collagenase for 24h at 37°C). After digestion, we cultured the cells on 2D tissue culture plastic in standard culture medium and used the resulting mixed fibroblast progenitor population between passage 2 and 4. All medium components were purchased from Sigma Aldrich, except for the ascorbic acid (Wako Chemicals) and the collagenase (ThermoFisher).

Collagen isolation

We isolated collagen-1 from rat tail tendon fascicles following an established protocol.[79]

Hydrogel preparation, core explant embedding, and assembloid culture

As described previously,[51] core explants were fixated with clamps, placed into molds lining silicone chambers, and tensioned. These molds were then filled with cell-free or progenitor-laden collagen hydrogels. One hydrogel consisted of 10 µL PBS (20x), 1.28 µL of 1M NaOH (125x), 8.72 µL double-distilled water (ddH_2O, 23x), 80 µL collagen-1 (2.5x or 1.6 mg / ml) and 100 µL culture media or cell suspension (2x). All hydrogel components were kept on ice to prevent pre-mature crosslinking. Co-culture medium (DMEM/F12 high glucose, 10% FBS, 1% non-essential amino acids, 1% Penicillin / Streptomycin, 1% Amphotericin, 200 µM L-Ascorbic Acid, 20 ng/ml macrophage-colony stimulating factor) was added to stable hydrogels after 50 min of polymerization at 37°C and tension was released. The assembloids were then cultured under lesion-like niche conditions (37°C, 20% O_2) with two media changes per week until the determined timepoint.[68] We used a final concentration of 25 ng/ml recombinant IL-6 (PeproTech, 216-16) in those assembloids to be stimulated by it, and a final concentration of 10 µg/ml Tocilizumab (TargetMol, T9911) in those assembloids to be inhibited by it.

RNA isolation for genome-wide RNA sequencing (bulk RNA-seq)

We pooled 20 – 24x 2 cm core explants and 2 progenitor-laden collagen hydrogels separate from each other and snap-froze them in liquid nitrogen. The core explant pools were generated from a single mouse and represent one biological replicate each. The collagen hydrogel pools contained a mixed population comprising migratory cells from the embedded core (same mouse) and the initially seeded mixed progenitor population (cells pooled from 6 mice). The frozen samples were pulverized by cryogenic grinding (FreezerMill 6870, SPEX™SamplePrep) and further processed with the RNeasy micro kit (Qiagen) according to the manufacturer's instructions. We used the Nanodrop 1000 spectrophotometer 3.7.1 (ThermoFisher) to measure RNA concentration and purity, and the 4200 TapeStation System (Agilent) to measure RNA quality. For each condition (WT core // cell-free, WT core // progenitors, KO core // progenitors), all 6 of the collagen hydrogels pools but only 4 of the core explant pools passed both integrity control (RIN ≥ 2) and had a sufficiently high RNA concentration (30 – 100 ng / µl) for genome-wide RNA sequencing.
We submitted those pools to the functional genomics center Zurich (https://fgcz.ch/, last visited 06.05.22) for the Illumina (Novaseq 6000) TruSeq TotalRNA stranded sequencing protocol

including library construction from total RNA using ribo-depletion, library QC, sequencing, and data delivery.

RNA-seq data processing and bioinformatic analysis

We used the R-based SUSHI framework of the Functional Genomics Center Zurich (ETH Zurich and University of Zurich) to perform primary level bioinformatics. Specifically, we used the FastqcApp, the FastqScreenApp, and the RnaBamStatsApp for quality control, the KallistoApp (sleuth) to calculate transcript abundance after pseudoalignment, the CountQCApp to quality control after counting reads, and the DESeq2App for differential expression analysis. We then used the shiny toolset developed by the Functional Genomics Center Zurich (https://github.com/fgcz/bfabricShiny, last visited 06.05.22) based on b-fabric and R to generate the annotated volcano plots, heatmaps, and gene set functional enrichment by applying the hypergeometric overrepresentation analysis (ORA) with the following settings:

Volcano plot:

Comparison	**P-value**	**P-value threshold**	**Log2 fc threshold**
Core of WT core // cell-free – Core of WT core // progenitors	FDR-adjusted	0.05	0.5
Core of WT core // progenitors – Core of KO core // progenitors	Raw	0.05	0.5
Progenitors from WT core // progenitors – Progenitors from KO core // progenitors	Raw	0.05	0.5

Heatmap:

Comparison	**#Genes**	**Scale**	**Count method**
WT core // cell-free – WT core // progenitors	Top 50 up & down	Diverging	Normalized + Log2
Core of WT core // progenitors – Core of KO core // progenitors	Top 50 up & down	Diverging	Normalized + Log2
Progenitors from WT core // progenitors – Progenitors from KO core // progenitors	Top 50 up & down	Diverging	Normalized + Log2

Overrepresentation analysis:

Comparison	**Input p-value**	**Output p-value**
WT core // cell-free – WT core // progenitors	FDR-adjusted < 0.01	FDR-adjusted < 0.05
Core of WT core // progenitors – Core of KO core // progenitors	Raw < 0.01	FDR-adjusted < 0.05
Progenitors from WT core // progenitors – Progenitors from KO core // progenitors	Raw < 0.01	FDR-adjusted < 0.05

We also looked at the increased (logFC > 0) and decreased (logFC < 0) transcripts in isolation to estimate their contribution to the enrichment and give it directionality. The emapplot of enriched biological processes independent of increased and decreased transcripts was generated in RStudio using the enrichPlot package.

We again used RStudio and the clusterProfiler package to perform the GSEA, taking the mouse hallmark and the cell type signature gene set annotations from the molecular signature database

(MSigDB, https://www.gsea-msigdb.org/gsea/msigdb/, last visited: 31.10.22) as reference after ranking the genes according to their signed log2 ratio. We used the following input parameters: pvalueCutoff = 1.00, minGSSize = 15, maxGSSize = 500, and eps = 0. Lastly, we used the gseaplot and dotplot functions from the enrichPlot package to plot the data and the sign of the enrichment score / NES to estimate the directionality.
The RNA sequencing data gathered from assembloids as discussed in this publication have been deposited in NCBI's Gene Expression Omnibus[80] and are accessible through GEO series accession number GSE214015 (https://www.ncbi.nlm.nih.gov/geo/query/acc.cgi?acc=GSE214015).
The *in vivo* mouse RNA sequencing data comparing paratenon-derived to tendon proper-derived progenitors have previously been published in an open access database (PRJNA399554, https://www.ncbi.nlm.nih.gov/bioproject/?term=PRJNA399554).[21] To reanalyze this data, we used the same tools and parameters as for the assembloid analysis (GO input: FDR-adjusted p-value < 0.01). The overlapping DEGs and GO terms were calculated and the resulting Venn-diagrams plotted with basic RStudio functions (i.e intersect & draw.pairwise.venn).

Quantifying total cell proliferation, ScxGFP$^+$ cell proliferation, and ScxGFP$^+$ cell recruitment to WT and KO core explants

In the assembloids used here, core explants from wildtype (WT) and homozygous (KO) B6.129S2-Il6tm1Kopf/J Il-6$^{-/-}$ mice were embedded with ScxGFP$^+$ progenitors from homo- and heterozygous Tgf(Scx-GFP)1Stzr mice. After seven days, the assembloids were removed from the clamps and washed with PBS before staining them with Ethidium Homodimer (EthD-1, Sigma-Aldrich, 2 mM stock in DMSO) diluted to 4 µM with PBS (20 min, 37°C). They were then again washed with PBS, fixated with 4% formaldehyde (Roti-Histofix, Karlsruhe) for 1 hour at room temperature, washed again with PBS, and stored in PBS at 4°C. Immediately before the imaging, nuclei were stained with NucBlue Live Ready Probes Reagent™ (R37605, ThermoFisher) for 1 hour at room temperature. We used the Nikon Eclipse T*i*2 confocal scanning microscope controlled by NIS-Elements to acquire the images (3 per sample), which we then processed with ImageJ 1.53q. Briefly, we first registered all cell locations by creating a mask from the NucBlue channel. Then, we put this mask over the ScxGFP-channel and measured the fluorescence intensity at the identified cell locations. We then transferred the signal intensity per location data to RStudio, where we first calculated the total cell numbers of all the images of one sample combined and normalized them to the wildtype median. Afterwards, we determined the fluorescence threshold for the ScxGFP-signal (using density plots and a negative control image) and applied this threshold to the dataset. We then calculated the total ScxGFP$^+$ cell numbers for each sample and normalized them to the wildtype median. Finally, we combined the cell location with the fluorescence intensity data to find the distance from the core where most of the ScxGFP$^+$ cells were located and to calculate the ratio between ScxGFP$^+$ present at the core and those present in the surrounding extrinsic hydrogel.

Quantifying mechanical properties of assembloids

We mounted the assembloids to a custom-made uniaxial stretching device equipped with a load cell as described previously[51]. After five cycles of pre-conditioning to 1% L_0, the assembloids were then stretched up to 2% L_0 to measure the linear elastic modulus (Emod) with a pre-load of 0.03 N. This measurement was repeated after 21 days (d21) of culture. We used Matlab R2017a and RStudio to read-out the linear elastic modulus and normalize it to the measurement immediately

after assembloid fabrication (d0). Media was changed every 2-3 days. For the corresponding condition, the core explants were devitalized by snap-freezing them repeatedly in liquid nitrogen.

Achilles tenotomy

Adult wildtype and homozygous *B6.129S2-Il6tm1Kopf/J* IL-6$^{-/-}$ mice[65] (between 12- and 15-weeks old) of both genders were anesthetized by isoflurane inhalation. While the mice were anesthetized, we transected the Achilles tendon of the right hindlimb by creating a small incision in the tendon midsubstance (**Figure 5A**). The contralateral hindlimb was used as the undamaged control. After the surgical intervention, we closed the skin wound with an 8/O prolene suture (Ethicon, W8703) and administered an analgesic (Buprenorphine, 0.1 mg/kg s.c., 26G needle). At one-week post-tenotomy, we euthanized the mice with CO_2. We collected the plantaris and Achilles tendon/ neotendon from both hindlegs for histology. The isolated tissues were placed in OCT (TissueTek), cooled down on dry ice, and then stored at -80°C until further use.

Immunofluorescence microscopy of Achilles tendon sections

We cut transversal cryosections (10 µm thickness) using a low-profile microtome blade (DB80 LX, BioSys Laboratories), collected them on a glass slide, and let them dry for 1h before storing them at -80°C until further use. Prior to staining, sections were air-dried for 30 min at RT (room temperature) and washed 3x with PBS for 5 min each. Then, sections were permeabilized and blocked with 3% BSA (bovine serum albumin) in PBS-T (PBS + 0.1% TritonX) for 1 h at RT. We washed the sections again, added the primary antibody for Scx (abcam, ab58655, diluted 1:200 in PBS-T with 1% BSA), TPPP3 (Invitrogen, PA5-24925, 1:200), or CD146 (BIOSS, bs-1618R, 1:200) covered them with parafilm, and left them overnight in a humid chamber at 4°C. Afterwards, we washed them again (3x 5 min with PBS) before adding the matching secondary antibodies (diluted 1:200 in PBS with 1% BSA) to the samples as well as the secondary antibody controls.
The sections were then washed again (3x 5 min with PBS + 1x 5 min with ultra-pure water) before mounting the coverslip with ROTI®Mount FluorCare DAPI (Roth). We used the Nikon Eclipse T*i*2 confocal scanning microscope controlled by NIS-Elements for acquiring the images, which we then processed with ImageJ 1.53q and RStudio as described previously (see "Quantifying total cell proliferation, ScxGFP$^+$ cell proliferation, and ScxGFP$^+$ cell recruitment to WT and KO core explants"). To quantify the migration through the location of Scx$^+$ / TPPP$^+$ / CD146$^+$ cells, we defined the lesional Achilles tendon area as a circle with a 480 µm radius set in the center of the Achilles tendon.

Statistical analysis and graph design

Data curation, statistical analysis, and plotting was done in RStudio ("Prairie Trillium", 9f796939, 2022-02-16) running R version 4.1.2. For normally distributed datasets, statistical information was obtained by ANOVA followed by Tukey Post-Hoc tests for pairwise comparisons. Else, the non-parametric Wilcoxon Rank Sum test was applied, directionally matching the data (less, greater, two-sided). For all tests, we tested the level of p-values. The mean and the standard error of the mean (sem) were reported for the following data: cumulative percentages of ScxGFP$^+$ progenitor cells in assembloids, elastic modulus of the assembloids, and cumulative percentages of Scx$^+$ / TPPP$^+$ / CD146$^+$ cells in the *in vivo* tenotomy model. We used bar and/or point plots to depict the mean and error bars/bands to depict the sem. We reported the median and interquartile range (IQR) in assembloids for the total cell number, the number of ScxGFP$^+$ cells, and the ratio between core-resident and extrinsic ScxGFP$^+$ cells, as well as for the total cell

number, the number of Scx^+ cells, and the ratio between Achilles and neotendon-resident Scx^+ / $TPPP^+$ / $CD146^+$ cells in the *in vivo* tenotomy. These values were depicted as boxplots with the upper and lower hinges corresponding to the first and third quartile (25th and 75th percentile), the middle one to the median, the whiskers extending from the upper/lower hinge to the largest/smallest value no further than 1.5 times the interquartile range, and dots representing data beyond the whiskers. Results of the statistical analysis are indicated as follows: $*p < 0.05$, $**p < 0.01$, $***p < 0.01$.

The open-source graphics software Inkscape 0.92.3 (www.inkscape.org, last visited 09.05.22) was used to finalize the graph design.

ACKNOWLEDGEMENTS

This work was funded by the ETH Grant 1-005733.
Declarations of interest: none

We would like to thank the Functional Genomics Center Zurich, and in particular Lennart Opitz and Dr. Maria Domenica Moccia, for their support on the RNA sequencing data analysis and Dr. Roberto Fiore from the System Neuroscience Lab at ETH Zurich for providing the rat tails for the collagen-1 extraction. We further acknowledge Dr. Evi Masschelein for performing the Achilles tenotomies and the Laboratory of Nutrition and Metabolic Epigenetics for the access to their Tapestation. We also thank our own Lab Technicians Barbara Niederöst and Maja Bollhalder for their practical and emotional support. Finally, we thank Dr. Knut Husmann and Dr. Annamari Katariina Alitalo for their help and support with obtaining the license for animal experimentation and animal husbandry.

SUPPORTING INFORMATION

GEO accession number	Sex	Source tissue	Age	Donor number	Disease state
GSM639748	Male	Tendon;Brachialis	45	5	Normal
GSM639749	Male	Tendon;EDC	48	9	Normal
GSM639750	Male	Tendon;Quadriceps	41	10	Normal
GSM639751	Male	Tendon;Flexor-Pronator	62	12	Normal
GSM639752	Female	Tendon;Subscapularis	62	13	Normal
GSM639753	Male	Tendon;Patellar	32	15	Normal
GSM639754	Female	Tendon;Subscapularis	61	16	Normal
GSM639755	Male	Tendon;Subscapularis	59	17	Normal
GSM639756	Male	Tendon;Flexor-Pronator	45	19	Normal
GSM639757	Female	Tendon;Subscapularis	63	20	Normal
GSM639758	Female	Tendon;Biceps	65	21	Normal
GSM639759	Female	Tendon;Subscapularis	64	23	Normal
GSM639760	Male	Tendon;Biceps	50	24	Normal
GSM639761	Male	Tendon;ECRB	55	26	Normal
GSM639762	Male	Tendon;Subscapularis	50	27	Normal
GSM639763	Male	Tendon;Biceps	41	28	Normal
GSM639764	Male	Tendon;Biceps	46	29	Normal
GSM639765	Male	Tendon;ECRL	52	30	Normal
GSM639766	Male	Tendon;Subscapularis	66	31	Normal
GSM639767	Female	Tendon;Teres minor	46	32	Normal
GSM639768	Male	Tendon;Subscapularis	44	33	Normal
GSM639769	Female	Tendon;Biceps	59	34	Normal
GSM639770	Female	Tendon;Subscapularis	49	35	Normal
GSM639771	Male	Tendon;Biceps	45	5	Tendinopathic
GSM639772	Male	Tendon;ECRB	48	9	Tendinopathic
GSM639773	Male	Tendon;Patellar	41	10	Tendinopathic
GSM639774	Male	Tendon;Flexor-Pronator	62	12	Tendinopathic
GSM639775	Female	Tendon;Suspraspinatus	62	13	Tendinopathic
GSM639776	Male	Tendon;Patellar	32	15	Tendinopathic
GSM639777	Female	Tendon;Suspraspinatus	61	16	Tendinopathic
GSM639778	Male	Tendon;Suspraspinatus	59	17	Tendinopathic
GSM639779	Male	Tendon;Flexor-Pronator	45	19	Tendinopathic
GSM639780	Female	Tendon;Suspraspinatus	63	20	Tendinopathic
GSM639781	Female	Tendon;Suspraspinatus	65	21	Tendinopathic
GSM639782	Female	Tendon;Suspraspinatus	64	23	Tendinopathic
GSM639783	Male	Tendon;Suspraspinatus	50	24	Tendinopathic
GSM639784	Male	Tendon;ECRB	55	26	Tendinopathic
GSM639785	Male	Tendon;Suspraspinatus	50	27	Tendinopathic
GSM639786	Male	Tendon;Suspraspinatus	41	28	Tendinopathic

GSM639787	Male	Tendon;Suspraspinatus	46	29	Tendinopathic
GSM639788	Male	Tendon;ECRB	52	30	Tendinopathic
GSM639789	Male	Tendon;Suspraspinatus	66	31	Tendinopathic
GSM639790	Female	Tendon;Suspraspinatus	46	32	Tendinopathic
GSM639791	Male	Tendon;Suspraspinatus	44	33	Tendinopathic
GSM639792	Female	Tendon;Suspraspinatus	59	34	Tendinopathic
GSM639793	Female	Tendon;Suspraspinatus	49	35	Tendinopathic

Supplementary Table 1: Human patient metadata. GEO accession number, patient sex, source tissue, patient age, donor number, and disease state of the isolated tissue ordered by GEO accession number. Samples colored in red were considered as outliers and as such excluded from further analysis.

A
Tendinopathic
Normal
PC2
PC1
200
100
0
-100
-100
0
100
200
Subscapularis
Teres minor
Subscapularis
Suspraspinatus
Subscapularis
Biceps
Biceps
Patella
Subscapularis
Suspraspinatus
Biceps
Subscapularis
Suspraspinatus
Suspraspinatus
Subscapularis
Suspraspinatus
ECRB
Suspraspinatus
Suspraspinatus
Biceps
Suspraspinatus
ECRB
Subscapularis
Suspraspinatus
Flexor−Pronator
Suspraspinatus
Biceps
Suspraspinatus
Subscapularis
Suspraspinatus
EDC
Subscapularis
Quadriceps
Suspraspinatus
Suspraspinatus
ECRB
Flexor−Pronator
Patella
Patella
Brachialis
ECRB
ECRL
Flexor−Pronator
Flexor−Pronator

B
Tendinopathic
Normal
PC2
PC1
100
0
-100
-200
-100
0
100
Subscapularis
Subscapularis
Quadriceps
EDC
Patella
Suspraspinatus
Flexor−Pronator
Biceps
Biceps
Biceps
Suspraspinatus
Suspraspinatus
Suspraspinatus
Suspraspinatus
Flexor−Pronator
Subscapularis
Suspraspinatus
Suspraspinatus
Subscapularis
ECRB
ECRB
Suspraspinatus
Biceps
Subscapularis
Suspraspinatus
Patella
Suspraspinatus
Biceps
Biceps
Suspraspinatus
Subscapularis
Teres Minor
Subscapularis

Supplementary Figure 2: PCA plots of the human tendon microarray data. (A) Principal components 1 and 2 for the full dataset with tendinopathic (red) and normal (blue) tendons. (B) Principal components 1 and 2 for the same dataset after excluding outliers based on tendon subtype and clustering in A.

A GO: Enriched biological processes

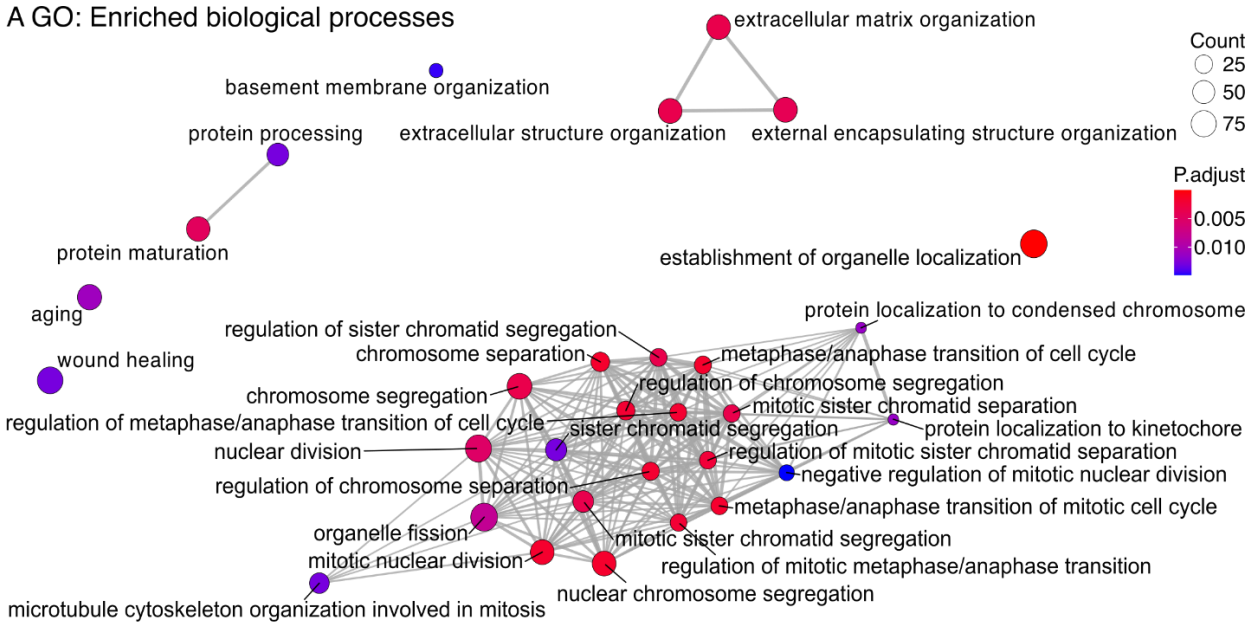

B & C Top 20 GO biological processes enriched by:

B Transcripts increased in tendinopathic tendons

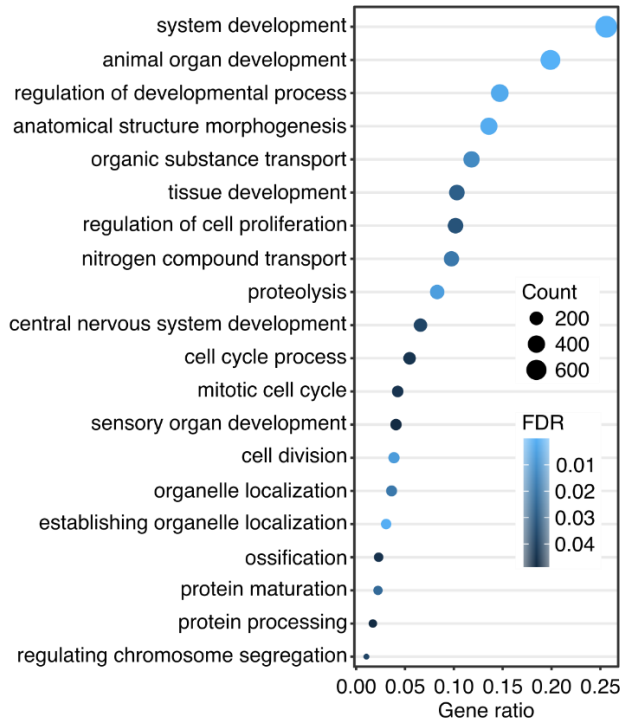

C Transcripts decreased in tendinopathic tendons

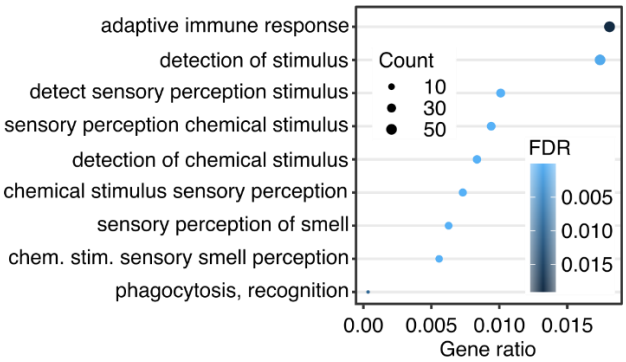

D & E Top 20 GO molecular functions enriched by:

D Transcripts increased in tendinopathic tendons

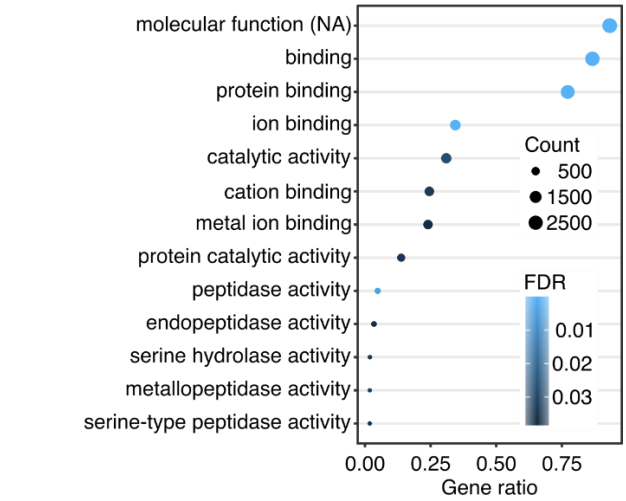

E Transcripts decreased in tendinopathic tendons

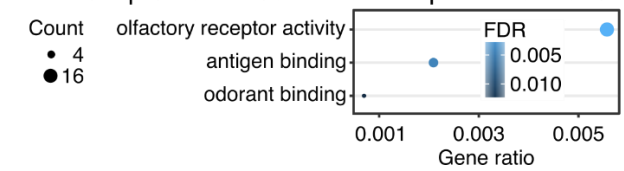

Supplementary Figure 3: Detailed transcriptome analysis of up- and downregulated genes and pathways in normal and human tendinopathic tendons. (A) Detailed annotation of the enrichment map plot clustering the top 30 biological processes significantly enriched by overlapping DEG sets. The color of the circles represents their adjusted p-values, the size represents the number of enriched genes (count), and the grey lines connect GO annotations that share the same gene subsets. (B) Dotplot showing the top 20 GO gene sets for biological processes significantly enriched by transcripts increased in human tendinopathic tendons. (C) Dotplot showing all the GO gene sets for biological processes enriched by transcripts decreased in human tendinopathic tendons. (D) Dotplot showing all the GO gene sets for molecular functions enriched by transcripts increased in human tendinopathic tendons. (E) Dotplot showing all the GO gene sets for molecular functions enriched by transcripts decreased in human tendinopathic tendons. In all the dotplots, the color of the circles represents their adjusted p-value, the size the number of enriched genes (count), and the position on the x-axis the number of enriched genes in ratio to the total number of genes annotated to the gene set (gene ratio).

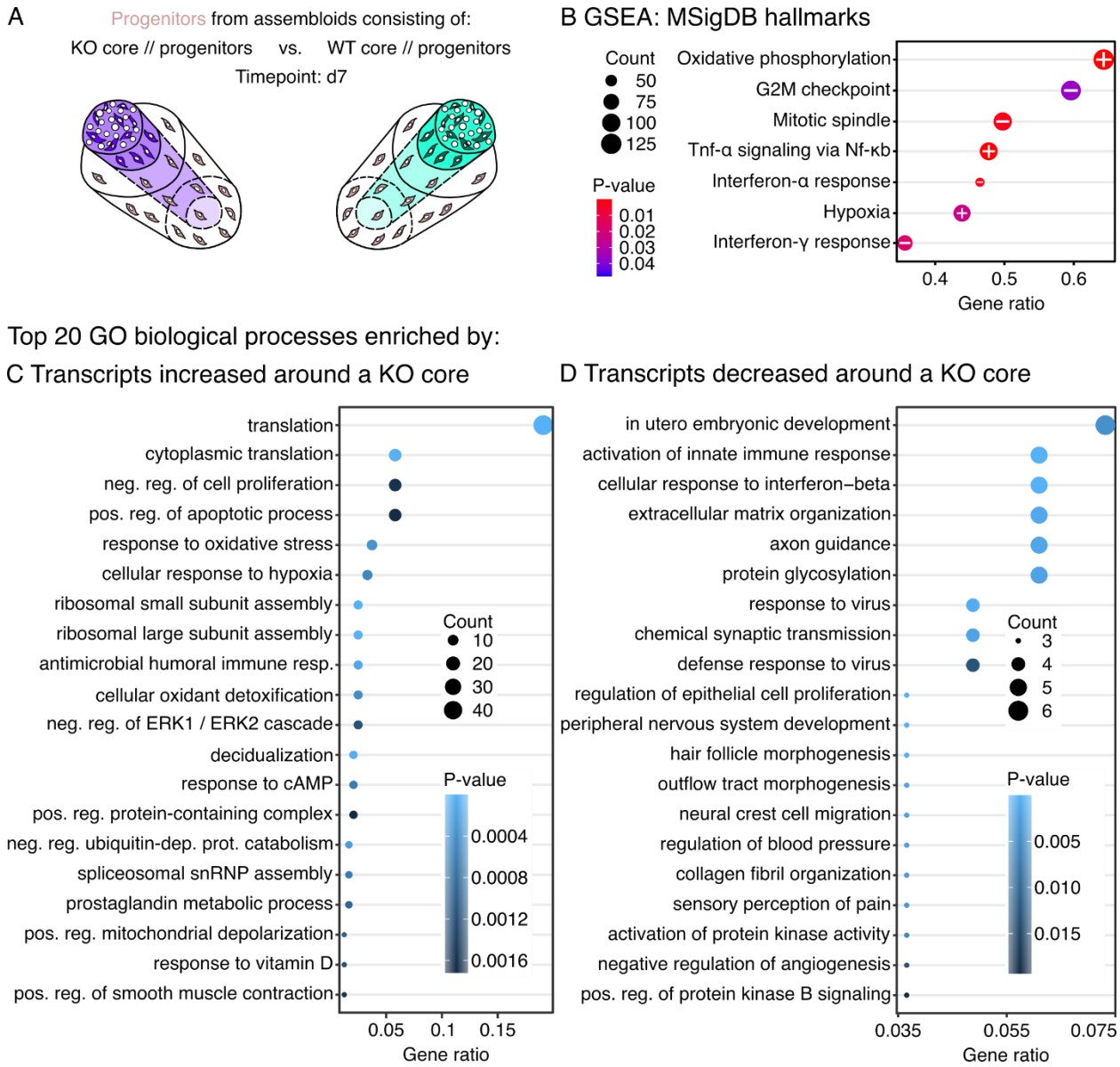

Supplementary Figure 4: Detailed transcriptome analysis of genes up- and down-regulated in hydrogel-embedded fibroblast progenitors seeded around an IL-6 knock-out (KO) core explant compared to those seeded around a wildtype (WT) core. (A) Illustration of the assembloid combinations compared here (KO core // progenitors vs. WT core // progenitors), the assessed timepoint (d7), and the analyzed compartment (extrinsic fibroblast progenitors only). (B) Dotplot showing significantly enriched gene sets (p-value < 0.05) as determined by GSEA based on the MSigDB mouse hallmark gene sets. The +/- signs indicate the direction of the enrichment. (C) Dotplot showing the top 20 GO gene sets for biological processes significantly enriched by transcripts increased in fibroblast progenitors seeded around a KO core. (D) Dotplot showing the top 20 GO gene sets for biological processes significantly enriched by transcripts decreased in fibroblast progenitors seeded around a KO core. In all the dotplots, the color of the circles represents their p-value, the size the number of enriched genes (count), and the position on the x-axis the number of enriched genes in ratio to the total number of genes annotated to the gene set (gene ratio).

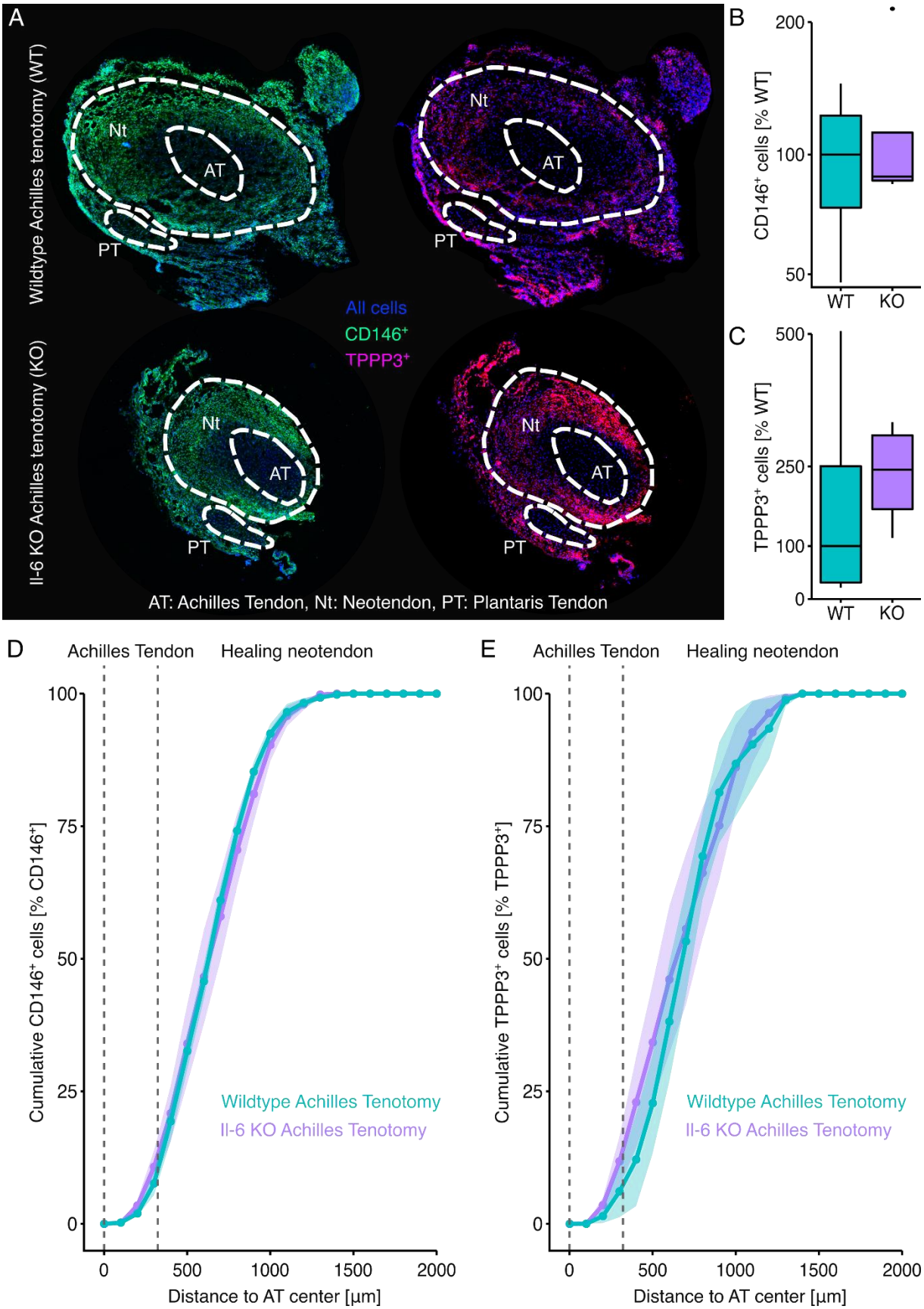
A
Wildtype Achilles tenotomy (WT)
Il-6 KO Achilles tenotomy (KO)
Nt
AT
PT
All cells
CD146⁺
TPPP3⁺
AT: Achilles Tendon, Nt: Neotendon, PT: Plantaris Tendon
B
CD146⁺ cells [% WT]
200
100
50
WT
KO
C
TPPP3⁺ cells [% WT]
500
250
100
0
WT
KO
D
Achilles Tendon
Healing neotendon
Cumulative CD146⁺ cells [% CD146⁺]
Wildtype Achilles Tenotomy
Il-6 KO Achilles Tenotomy
Distance to AT center [µm]
E
Achilles Tendon
Healing neotendon
Cumulative TPPP3⁺ cells [% TPPP3⁺]
Wildtype Achilles Tenotomy
Il-6 KO Achilles Tenotomy
Distance to AT center [µm]

Supplementary Figure 5: CD146+ and TPPP3+ fibroblast progenitor recruitment to damaged mouse Achilles tendons. (A) Representative fluorescence microscopy images of mouse hindleg sections from wildtype (WT) and IL-6 knock-out (KO) Achilles tendons that underwent unilateral tenotomy. (B) Boxplot reporting the number of CD146+ cells normalized to the WT median. (C) Boxplot reporting the number of TPPP3+ cells normalized to the WT median. In these boxplots, the upper and lower hinges correspond to the first and third quartile (25th and 75th percentile), the middle one to the median, the whiskers extend from the hinges no further than 1.5 times the interquartile range, and the points beyond the whiskers are treated as outliers. (D, E) Lineplots depicting the cumulative percentages of CD146+ and TPPP3+ cells depending on their distance from the Achilles tendon center. The points and the line represent the mean cumulative percentages and the error bands their standard error of the mean (sem). The dashed line indicates locations inside the Achilles tendon stump. N=4. The applied statistical test was the non-parametric Wilcoxon Rank Sum Test and no significant differences were detected.

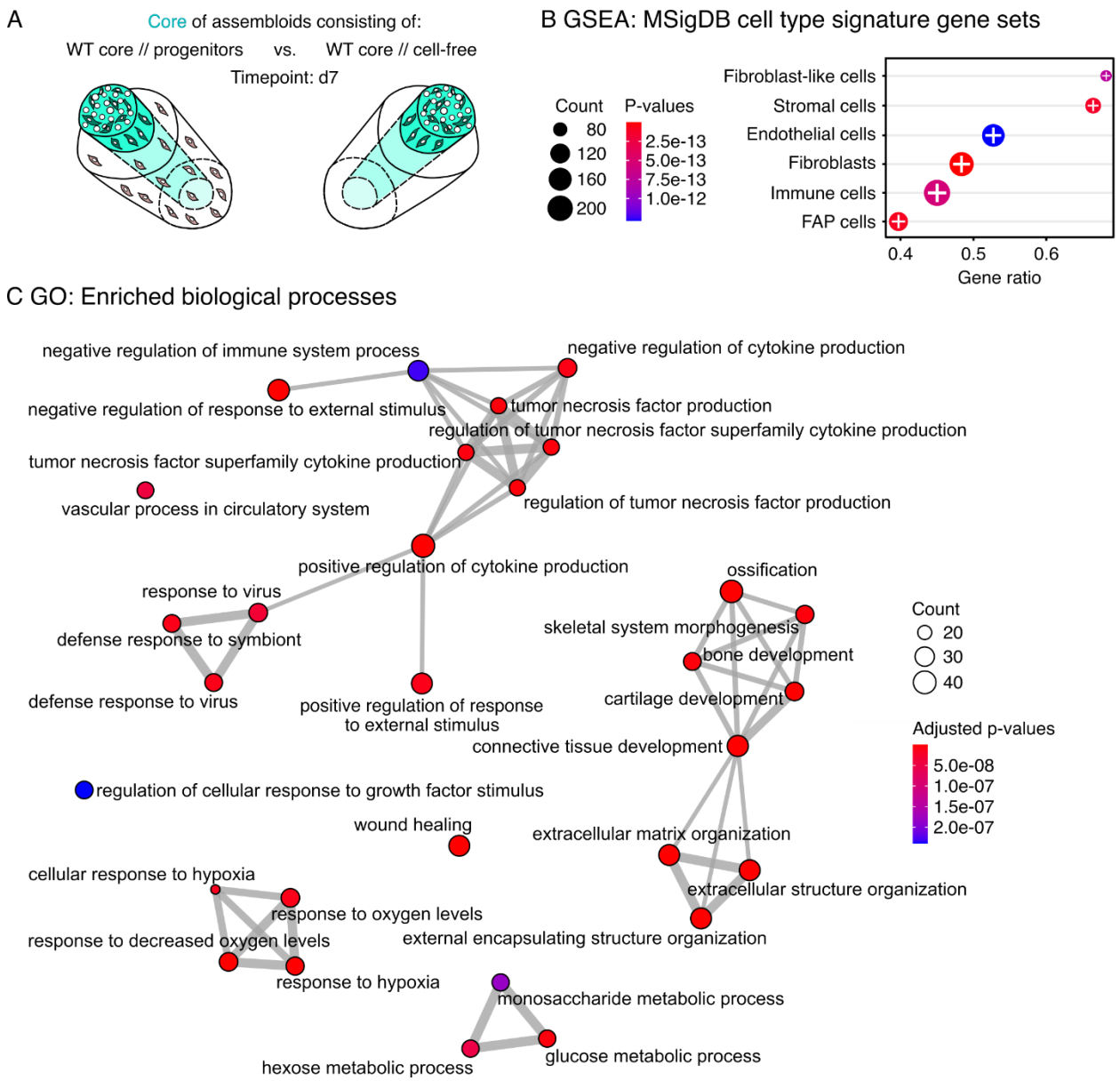

Supplementary Figure 6: Detailed transcriptome analysis of genes up- and down-regulated in wildtype (WT) core explants surrounded by a hydrogel seeded with fibroblast progenitors compared to a WT core surrounded by a cell-free hydrogel. (A) Illustration of the assembloid combinations compared here (WT core // progenitors vs. WT core // cell-free), the assessed timepoint (d7), and the analyzed compartment (core only). (B) Dotplot depicting the top 6 significantly enriched gene sets as determined by GSEA based on the MSigDB mouse cell type signature gene sets. The color of the circles represents their p-value, the size the number of enriched genes (count), the position on the x-axis the number of enriched genes in ratio to the total number of genes annotated to the gene set (gene ratio), and the +/- signs the direction of the enrichment. (C) Detailed annotation of the enrichment map plot clustering the top 30 biological processes significantly enriched by DEG sets. The color of the circles represents their adjusted p-values, the size represents the number of enriched genes (count), and the grey lines connect GO annotations that share the same gene subsets.

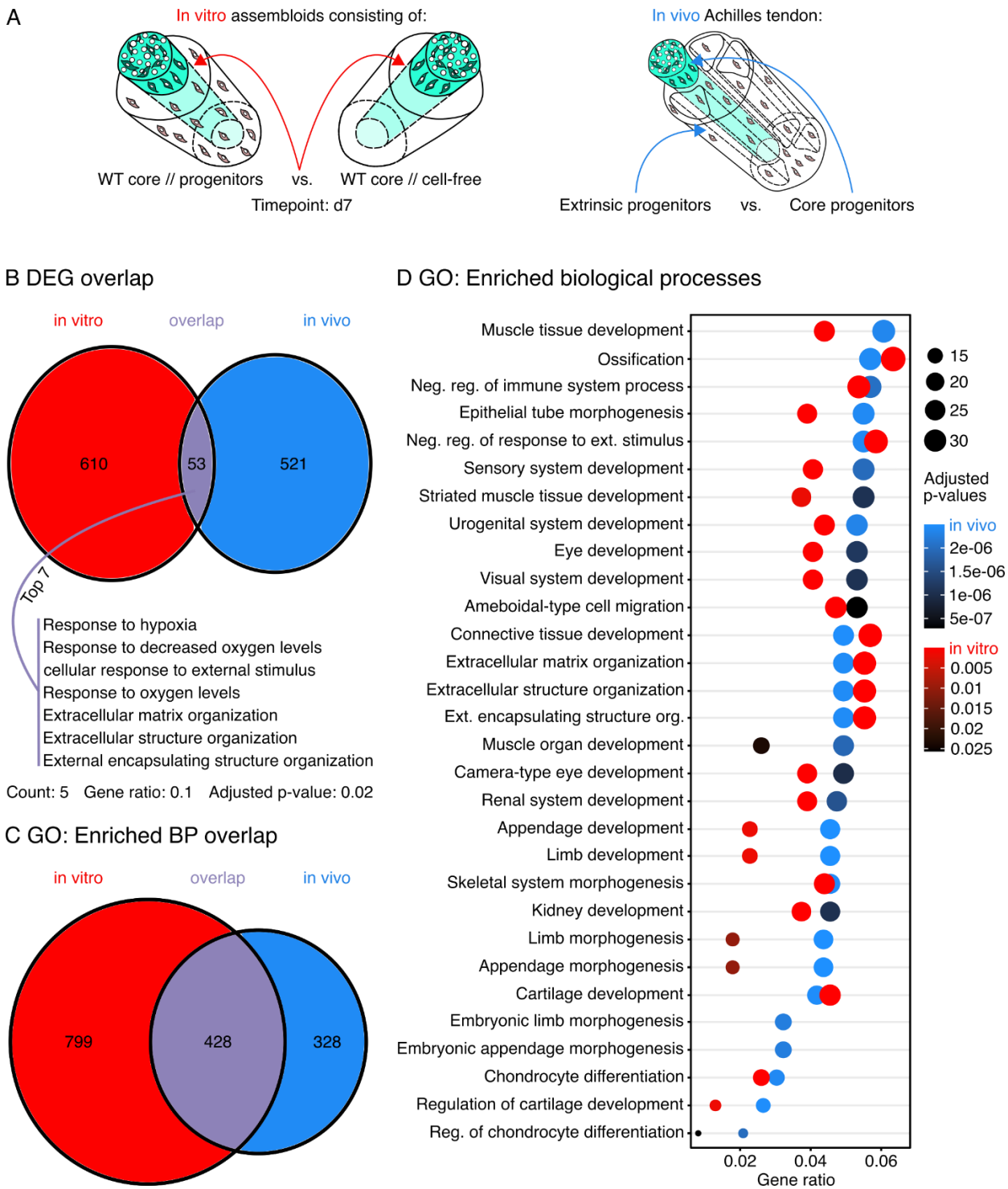

Supplementary Figure 7: Overlap between differentially expressed transcripts in in vitro assembloids and differentially expressed transcripts between Achilles tendon fibroblast progenitors from the extrinsic compartment and the tendon core in vivo. (A) Illustrative depiction of the comparisons whose overlap was investigated here: The core explants of WT core // progenitor vs. the WT core // cell-free progenitor assembloids (in vitro, red) and the extrinsic (paratenon-derived) vs. the core (tendon proper-derived) fibroblast progenitors (in vivo, blue). (B) Venn-Diagramm depicting the number and the overlap (violet) of DEGs as well as the top 7 GO gene sets for biological processes significantly enriched by the overlapping DEGs. (C) Venn-Diagramm depicting the number and the overlap (violet) of significantly enriched GO annotations for biological processes. (D) Dotplot depicting the top 30 biological processes significantly enriched by DEGs in tendon fibroblast progenitors derived from the extrinsic

compartment (paratenon-derived) compared to those derived from the core compartment (tendon proper-derived) colored in a blue to black gradient. The plot is augmented by the data of matched biological processes also significantly enriched in the core of WT core // progenitor compared to that of the WT core // cell-free progenitor assembloids colored in a red to black gradient. The color gradient of the circles represents their adjusted p-values, the size the number of enriched genes (count), and the x-axis the number of enriched genes in ratio to the total number of genes annotated to the gene set (gene ratio).

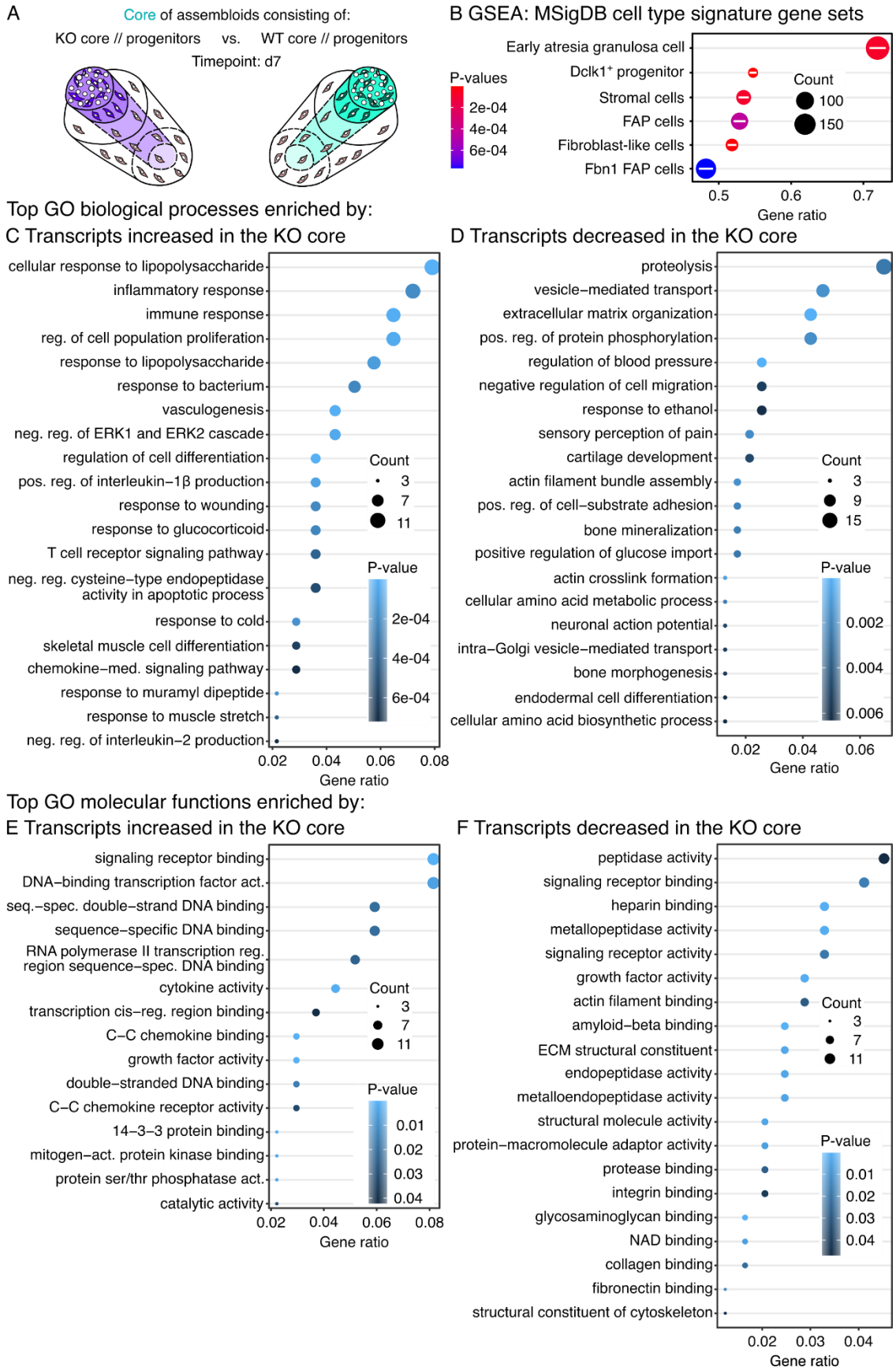
A
Core of assembloids consisting of:
KO core // progenitors vs. WT core // progenitors
Timepoint: d7
B GSEA: MSigDB cell type signature gene sets
P-values
2e-04
4e-04
6e-04
Early atresia granulosa cell
Dclk1+ progenitor
Stromal cells
FAP cells
Fibroblast-like cells
Fbn1 FAP cells
Count
100
150
0.5
0.6
0.7
Gene ratio
Top GO biological processes enriched by:
C Transcripts increased in the KO core
cellular response to lipopolysaccharide
inflammatory response
immune response
reg. of cell population proliferation
response to lipopolysaccharide
response to bacterium
vasculogenesis
neg. reg. of ERK1 and ERK2 cascade
regulation of cell differentiation
pos. reg. of interleukin−1β production
response to wounding
response to glucocorticoid
T cell receptor signaling pathway
neg. reg. cysteine−type endopeptidase activity in apoptotic process
response to cold
skeletal muscle cell differentiation
chemokine−med. signaling pathway
response to muramyl dipeptide
response to muscle stretch
neg. reg. of interleukin−2 production
Count
3
7
11
P-value
2e-04
4e-04
6e-04
0.02
0.04
0.06
0.08
Gene ratio
D Transcripts decreased in the KO core
proteolysis
vesicle−mediated transport
extracellular matrix organization
pos. reg. of protein phosphorylation
regulation of blood pressure
negative regulation of cell migration
response to ethanol
sensory perception of pain
cartilage development
actin filament bundle assembly
pos. reg. of cell−substrate adhesion
bone mineralization
positive regulation of glucose import
actin crosslink formation
cellular amino acid metabolic process
neuronal action potential
intra−Golgi vesicle−mediated transport
bone morphogenesis
endodermal cell differentiation
cellular amino acid biosynthetic process
Count
3
9
15
P-value
0.002
0.004
0.006
0.02
0.04
0.06
Gene ratio
Top GO molecular functions enriched by:
E Transcripts increased in the KO core
signaling receptor binding
DNA−binding transcription factor act.
seq.−spec. double−strand DNA binding
sequence−specific DNA binding
RNA polymerase II transcription reg. region sequence−spec. DNA binding
cytokine activity
transcription cis−reg. region binding
C−C chemokine binding
growth factor activity
double−stranded DNA binding
C−C chemokine receptor activity
14−3−3 protein binding
mitogen−act. protein kinase binding
protein ser/thr phosphatase act.
catalytic activity
Count
3
7
11
P-value
0.01
0.02
0.03
0.04
0.02
0.04
0.06
0.08
Gene ratio
F Transcripts decreased in the KO core
peptidase activity
signaling receptor binding
heparin binding
metallopeptidase activity
signaling receptor activity
growth factor activity
actin filament binding
amyloid−beta binding
ECM structural constituent
endopeptidase activity
metalloendopeptidase activity
structural molecule activity
protein−macromolecule adaptor activity
protease binding
integrin binding
glycosaminoglycan binding
NAD binding
collagen binding
fibronectin binding
structural constituent of cytoskeleton
Count
3
7
11
P-value
0.01
0.02
0.03
0.04
0.02
0.03
0.04
Gene ratio

Supplementary Figure 8: Detailed transcriptome analysis of genes up- and down-regulated in knock-out (KO) core explants surrounded by a hydrogel seeded with fibroblast progenitors compared to a wildtype (WT) core surrounded by fibroblast progenitors. (A) Illustration depicting the assembloid combinations compared here (KO core // progenitors vs. WT core // progenitors), the assessed timepoint (d7), and the analyzed compartment (core only). (B) Dotplot depicting the top 6 significantly enriched gene sets as determined by GSEA based on the MSigDB mouse cell type signature gene sets. The +/- signs indicate the direction of the enrichment. (C) Dotplot showing the top 20 GO gene sets for biological processes significantly enriched by transcripts increased in the core of KO core // progenitor assembloids. (D) Dotplot showing the top 20 GO gene sets for biological processes significantly enriched by transcripts decreased in the core of KO core // progenitor assembloids. (E) Dotplot showing the top 20 GO gene sets for molecular functions significantly enriched by transcripts increased in the core of KO core // progenitor assembloids. (F) Dotplot showing the top 20 GO gene sets for molecular functions significantly enriched by transcripts decreased in the core of KO core // progenitor assembloids. In all the dotplots, the color of the circles represents their p-value, the size the number of enriched genes (count), and the position on the x-axis the number of enriched genes in ratio to the total number of genes annotated to the gene set (gene ratio).

REFERENCES

[1] D. T. Kirkendall, W. E. Garrett, *Scand. J. Med. Sci. Sport.* **1997**, *7*, 62.

[2] D. Florit, C. Pedret, M. Casals, P. Malliaras, D. Sugimoto, G. Rodas, *J. Sport. Sci. Med.* **2019**, *18*, 780.

[3] M. D. McElvany, E. McGoldrick, A. O. Gee, M. B. Neradilek, F. A. Matsen, *Am. J. Sports Med.* **2015**, *43*, 491.

[4] J. G. Snedeker, J. Foolen, *Acta Biomater.* **2017**, DOI 10.1016/j.actbio.2017.08.032.

[5] E. Yelin, S. Weinstein, T. King, *Semin. Arthritis Rheum.* **2016**, *46*, 259.

[6] K. Lipman, C. Wang, K. Ting, C. Soo, Z. Zheng, *Drug Des. Devel. Ther.* **2018**, *12*, 591.

[7] G. Riley, *Nat. Clin. Pract. Rheumatol.* **2008**, *4*, 82.

[8] L. J. Soslowsky, S. Thomopoulos, S. Tun, C. L. Flanagan, C. C. Keefer, J. Mastaw, J. E. Carpenter, *J. Shoulder Elb. Surg.* **2000**, *9*, 79.

[9] T. A. H. Järvinen, P. Kannus, N. Maffulli, K. M. Khan, *Foot Ankle Clin.* **2005**, *10*, 255.

[10] S. P. Magnusson, H. Langberg, M. Kjaer, *Nat. Rev. Rheumatol.* **2010**, *6*, 262.

[11] T. L. Willett, R. S. Labow, N. C. Avery, J. M. Lee, *Ann. Biomed. Eng.* **2007**, *35*, 1961.

[12] K. Howell, C. Chien, R. Bell, D. Laudier, S. F. Tufa, D. R. Keene, N. Andarawis-Puri, A. H. Huang, *Sci. Rep.* **2017**, *7*, 1.

[13] J. Li, J. Chen, R. Kirsner, *Clin. Dermatol.* **2007**, *25*, 9.

[14] N. L. Millar, K. G. Silbernagel, K. Thorborg, P. D. Kirwan, L. M. Galatz, G. D. Abrams, G. A. C. Murrell, I. B. McInnes, S. A. Rodeo, *Nat. Rev. Dis. Prim.* **2021**, *7*, DOI 10.1038/s41572-020-00234-1.

[15] R. H. Gelberman, P. R. Manske, W. Akeson, S. Woo, G. Lundborg, D. Amiel, *J. Orthop. Res.* **1986**, *4*, 119.

[16] P. Sharma, N. Maffulli, *J. Musculoskelet. Neuronal Interact.* **2006**, *6*, 181.

[17] T. Harvey, S. Flamenco, C. M. Fan, *Nat. Cell Biol.* **2019**, *21*, 1490.

[18] N. A. Dyment, C. F. Liu, N. Kazemi, L. E. Aschbacher-Smith, K. Kenter, A. P. Breidenbach, J. T. Shearn, C. Wylie, D. W. Rowe, D. L. Butler, *PLoS One* **2013**, *8*, DOI 10.1371/journal.pone.0059944.

[19] G. K. Tan, B. A. Pryce, A. Stabio, D. R. Keene, S. F. Tufa, R. Schweitzer, *Stem Cell Reports* **2021**, *16*, 2942.

[20] C. L. Mendias, J. P. Gumucio, K. I. Bakhurin, E. B. Lynch, S. V. Brooks, *J. Orthop. Res.* **2012**, *30*, 606.

[21] M. J. Mienaltowski, S. M. Adams, D. E. Birk, *Tissue Eng. - Part A* **2013**, *19*, 199.

[22] R. H. Gelberman, D. Steinberg, D. Amiel, W. Akeson, *J. Hand Surg. Am.* **1991**, *16*, 686.

[23] A. L. Serrano, B. Baeza-Raja, E. Perdiguero, M. Jardí, P. Muñoz-Cánoves, *Cell Metab.* **2008**, *7*, 33.

[24] H. Yin, F. Price, M. A. Rudnicki, *Physiol. Rev.* **2013**, *93*, 23.

[25] B. D. Cosgrove, A. Sacco, P. M. Gilbert, H. M. Blau, *Differentiation* **2009**, *78*, 185.

[26] L. C. Ceafalan, B. O. Popescu, M. E. Hinescu, *Biomed Res. Int.* **2014**, *2014*, DOI 10.1155/2014/957014.

[27] P. Muñoz-Cánoves, C. Scheele, B. K. Pedersen, A. L. Serrano, *FEBS J.* **2013**, *280*, 4131.

[28] T. Tanaka, M. Narazaki, T. Kishimoto, **2014**, *6*, 1.

[29] T. M. Kistner, B. K. Pedersen, D. E. Lieberman, *Nat. Metab.* **2022**, *4*, 170.

[30] H. Su, C. T. Lei, C. Zhang, *Front. Immunol.* **2017**, *8*, 1.

[31] P. Villar-Fincheira, F. Sanhueza-Olivares, I. Norambuena-Soto, N. Cancino-Arenas, F. Hernandez-Vargas, R. Troncoso, L. Gabrielli, M. Chiong, *Front. Mol. Biosci.* **2021**, *8*, 1.

[32] C. Zhang, Y. Li, Y. Wu, L. Wang, X. Wang, J. Du, *J. Biol. Chem.* **2013**, *288*, 1489.
[33] S. Watanabe, W. Mu, A. Kahn, N. Jing, J. H. Li, H. Y. Lan, T. Nakagawa, R. Ohashi, R. J. Johnson, *Am. J. Nephrol.* **2004**, *24*, 387.
[34] M. Ernst, B. J. Jenkins, *Trends Genet.* **2004**, *20*, 23.
[35] R. Eulenfeld, A. Dittrich, C. Khouri, P. J. Müller, B. Mütze, A. Wolf, F. Schaper, *Eur. J. Cell Biol.* **2012**, *91*, 486.
[36] E. Choy, S. Rose-John, *J. Scleroderma Relat. Disord.* **2017**, *2*, S1.
[37] E. Wada, J. Tanihata, A. Iwamura, S. Takeda, Y. K. Hayashi, R. Matsuda, *Skelet. Muscle* **2017**, *7*, 1.
[38] E. H. Choy, F. De Benedetti, T. Takeuchi, M. Hashizume, M. R. John, T. Kishimoto, *Nat. Rev. Rheumatol.* **2020**, *16*, 335.
[39] E. H. Choy, A. F. Kavanaugh, S. A. Jones, *Nat. Rev. Rheumatol.* **2013**, *9*, 154.
[40] S. Srirangan, E. H. Choy, *Ther. Adv. Musculoskelet. Dis.* **2010**, *2*, 247.
[41] R. T. Lewinson, I. A. Vallerand, L. M. Parsons, J. M. Lamothe, A. D. Frolkis, M. W. Lowerison, G. G. Kaplan, S. B. Patten, C. Barnabe, *RMD Open* **2018**, *4*, 1.
[42] C. De Simone, C. Guerriero, A. R. Giampietruzzi, M. Costantini, F. Di Gregorio, P. Amerio, *J. Am. Acad. Dermatol.* **2003**, *49*, 217.
[43] F. Poutoglidou, C. Pourzitaki, M. E. Manthou, E. Samoladas, A. Saitis, F. Malliou, D. Kouvelas, *Connect. Tissue Res.* **2022**, *00*, 1.
[44] E. H. S. Choy, D. A. Isenberg, T. Garrood, S. Farrow, Y. Ioannou, H. Bird, N. Cheung, B. Williams, B. Hazleman, R. Price, et al., *Arthritis Rheum.* **2002**, *46*, 3143.
[45] P. Emery, E. Keystone, H. P. Tony, A. Cantagrel, R. Van Vollenhoven, A. Sanchez, E. Alecock, J. Lee, J. Kremer, *Ann. Rheum. Dis.* **2008**, *67*, 1516.
[46] M. Colquhoun, M. Gulati, Z. Farah, M. Mouyis, *Medicine (Baltimore).* **2022**, *50*, 138.
[47] M. Åström, A. Rausing, *Clin. Orthop. Relat. Res.* **1995**, *NA;*, 151.
[48] G. Andersson, L. J. Backman, A. Scott, R. Lorentzon, S. Forsgren, P. Danielson, *Br. J. Sports Med.* **2011**, *45*, 1017.
[49] G. C. Jones, A. N. Corps, C. J. Pennington, I. M. Clark, D. R. Edwards, M. M. Bradley, B. L. Hazleman, G. P. Riley, *Arthritis Rheum.* **2006**, *54*, 832.
[50] G. P. Riley, R. L. Harrall, C. R. Constant, M. D. Chard, T. E. Cawston, B. L. Hazleman, *Ann. Rheum. Dis.* **1994**, *53*, 359.
[51] T. Stauber, M. Wolleb, A. Duss, P. K. Jaeger, I. Heggli, A. A. Hussien, U. Blache, J. G. Snedeker, *Adv. Healthc. Mater.* **2021**, *10*, 1.
[52] T. Sakabe, K. Sakai, T. Maeda, A. Sunaga, N. Furuta, R. Schweitzer, T. Sasaki, T. Sakai, *J. Biol. Chem.* **2018**, *293*, jbc. RA118.001987.
[53] T. Harvey, S. Flamenco, C.-M. Fan, *Nat. Cell Biol.* **2019**, *21*, DOI 10.1038/s41556-019-0417-z.
[54] T. W. Lin, L. Cardenas, D. L. Glaser, L. J. Soslowsky, *J. Biomech.* **2006**, *39*, 61.
[55] K. Nakama, M. Gotoh, T. Yamada, Y. Mitsui, H. Yasukawa, T. Imaizumi, F. Higuchi, K. Nagata, *J. Int. Med. Res.* **2006**, *34*, 624.
[56] T. Stauber, U. Blache, J. G. Snedeker, *Matrix Biol.* **2020**, *85–86*, DOI 10.1016/j.matbio.2019.07.008.
[57] K. Legerlotz, E. R. Jones, H. R. C. Screen, G. P. Riley, *Rheumatol. (United Kingdom)* **2012**, *51*, 1161.
[58] S. A. Jelinsky, S. A. Rodeo, J. Li, L. V. Gulotta, J. M. Archambault, H. J. Seeherman, *BMC Musculoskelet. Disord.* **2011**, *12*, DOI 10.1186/1471-2474-12-86.

[59] A. Subramanian, P. Tamayo, V. K. Mootha, S. Mukherjee, B. L. Ebert, M. A. Gillette, A. Paulovich, S. L. Pomeroy, T. R. Golub, E. S. Lander, et al., *Proc. Natl. Acad. Sci. U. S. A.* **2005**, *102*, 15545.
[60] A. Liberzon, C. Birger, H. Thorvaldsdóttir, M. Ghandi, J. P. Mesirov, P. Tamayo, *Cell Syst.* **2015**, *1*, 417.
[61] V. Moresi, S. Adamo, L. Berghella, *Front. Physiol.* **2019**, *10*, DOI 10.3389/fphys.2019.00500.
[62] M. A. Nowell, P. J. Richards, S. Horiuchi, N. Yamamoto, S. Rose-John, N. Topley, A. S. Williams, S. A. Jones, *J. Immunol.* **2003**, *171*, 3202.
[63] M. M. McFarland-Mancini, H. M. Funk, A. M. Paluch, M. Zhou, P. V. Giridhar, C. A. Mercer, S. C. Kozma, A. F. Drew, *J. Immunol.* **2010**, *184*, 7219.
[64] S. Tarafder, E. Chen, Y. Jun, K. Kao, K. H. Sim, J. Back, F. Y. Lee, C. H. Lee, *FASEB J.* **2017**, *31*, 3991.
[65] M. Kopf, H. Baumannt, G. Freer, M. Freudenberg, M. Lamers, T. K. Ii, R. Zinkernagel, H. Bluethmann, G. Kohler, **1994**, *368*, 815.
[66] M. J. Mienaltowski, A. Cánovas, V. A. Fates, A. R. Hampton, M. Y. Pechanec, A. Islas-Trejo, J. F. Medrano, *J. Orthop. Res.* **2019**, *37*, 1409.
[67] U. Blache, S. L. Wunderli, A. A. Hussien, T. Stauber, G. Flückiger, M. Bollhalder, B. Niederöst, S. F. Fucentese, J. G. Snedeker, *Sci. Rep.* **2021**, *11*, DOI 10.1038/s41598-021-85331-1.
[68] S. L. Wunderli, U. Blache, A. B. Piccoli, B. Niederöst, C. N. Holenstein, F. Passini, U. Silvan, L. Bundgaard, U. au dem Keller, J. G. Snedeker, *Matrix Biol.* **2020**.
[69] H. Langberg, J. L. Olesen, C. Gemmer, M. Kjær, *J. Physiol.* **2002**, *542*, 985.
[70] V. Arvind, A. H. Huang, *Front. Bioeng. Biotechnol.* **2021**, *9*, 1.
[71] S. Rose-John, *Int. J. Biol. Sci.* **2012**, *8*, 1237.
[72] N. A. Dyment, Y. Hagiwara, B. G. Matthews, Y. Li, I. Kalajzic, D. W. Rowe, *PLoS One* **2014**, *9*, DOI 10.1371/journal.pone.0096113.
[73] X. Niu, A. Subramanian, T. H. Hwang, T. F. Schilling, J. L. Galloway, *Curr. Biol.* **2020**, *30*, 3277.
[74] A. Korcari, A. E. C. Nichols, M. R. Buckley, A. E. Loiselle, **2022**.
[75] S. KB, L. J, G. JP, M. CL, *J. Orthop. Res.* **2014**, *32*, DOI 10.1002/JOR.22624.
[76] K. T. Best, A. Korcari, K. E. Mora, A. E. Nichols, S. N. Muscat, E. Knapp, M. R. Buckley, A. E. Loiselle, *Elife* **2021**, *10*, DOI 10.7554/eLife.62203.
[77] A. Korcari, S. Muscat, M. Buckley, A. L.- BioRxiv, U. 2022, *biorxiv.org* **2022**.
[78] S. Kult, T. Olender, M. Osterwalder, S. Markman, D. Leshkowitz, S. Krief, R. Blecher-Gonen, S. Ben-Moshe, L. Farack, H. Keren-Shaul, et al., *Elife* **2021**, *10*, 1.
[79] C. J. Doillon, D. Mantovani, N. Rajan, J. Habermehl, M. Cote, **2007**, *1*, 2753.
[80] R. Edgar, M. Domrachev, A. E. Lash, *Nucleic Acids Res.* **2002**, *30*, 207.